

**A Determination of the Effective Thickness of a
Liquid Deuterium Target for a Quasielastic
Scattering Experiment**

by

Jared Ripley Turkewitz

Submitted to the Department of Physics
in partial fulfillment of the requirements for the degree of

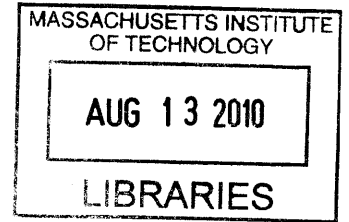
Bachelor of Science in Physics

at the


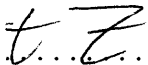
MASSACHUSETTS INSTITUTE OF TECHNOLOGY

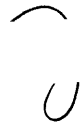
June 2010

© Massachusetts Institute of Technology 2010. All rights reserved.



ARCHIVES

Author  
Department of Physics
May 14, 2010

Certified by 
June L. Matthews
Professor
Thesis Supervisor

Accepted by 
David E. Pritchard
Senior Thesis Coordinator, Department of Physics

A Determination of the Effective Thickness of a Liquid Deuterium Target for a Quasielastic Scattering Experiment

by

Jared Ripley Turkewitz

Submitted to the Department of Physics
on May 14, 2010, in partial fulfillment of the
requirements for the degree of
Bachelor of Science in Physics

Abstract

The effective thickness of a liquid deuterium target was determined by measuring the yield of the neutron-deuteron elastic scattering cross section. The flux of incident neutrons was determined by a fission ionization chamber. The scattered deuterons were detected with a Delta E - E (thin plastic scintillator - thick CsI calorimeter) telescope. The effective target thickness was determined to be larger than is thought physically possible. Possible reasons for the unphysical result are discussed, but further analysis is needed to ascertain why the effective target thickness was determined to be an unphysical length.

Thesis Supervisor: June L. Matthews

Title: Professor

Acknowledgments

I would like to thank Professor June Matthews for her support and ability to quickly determine the heart of a problem. I am also extraordinarily thankful for the help and guidance provided by Vladimir Henzl. Vlad you were truly dedicated, patient and inspirational. Art Bridge, thanks for your work ethic and friendly personality; you were integral in the successful operation of this experiment. Professor Mark Yuly thanks for ensuring this experiment got started on the right foot. Also thanks to Katrina Koehler, Peter Kroening, Jonathan Slye and Sho Uemura who all worked tirelessly and maintained a positive attitude, even if things took more time than expected. Finally, I would like to thank my parents for the love and support you both have always given me.

Contents

1	Introduction	15
2	Experimental Setup	17
2.1	Overview of Experiment	17
2.2	Neutron Beam Production	17
2.3	Liquid Deuterium Target	19
2.4	Fission Chamber	20
2.5	Detectors	21
2.5.1	Proton Spectrometer	21
2.5.2	Neutron Detection	22
2.5.3	Charged Particle Telescope	22
3	Incident Neutron Flux	25
3.1	Fission Chamber Overview	25
3.2	Fission Chamber Time of Flight	25
3.2.1	Incident Neutron Kinetic Energy	27
3.3	Fission Chamber ADC Spectrum	28
3.4	Incident Neutron Flux	31
4	Effective Target Thickness	33
4.1	Principles of Effective Target Thickness	33
4.2	Effective Target Thickness	34
4.3	Live Time of the Data Acquisition System	35

4.4	Kinetic Energy of Incident Neutron and Elastically Scattered Deuteron from the ToF of the Neutron and Deuteron	36
4.5	Energy Loss in Target	37
5	Measurement of Elastically Scattered Deuteron	43
5.1	Identification of Elastically Scattered Deuteron	43
5.2	Total Time of Flight of the Neutron and Elastically Scattered	44
5.3	Number of Detected Deuterons as a Function of Incident Neutron Energy	47
5.3.1	DE2 ADC Cut for Elastically Scattered Deuterons	48
5.3.2	CsI ADC Cut for Elastically Scattered Deuterons	48
5.4	Determination of Background in Elastically Scattered Deuteron Detec- tion	51
5.5	Alternative Method for Determining Background in Scattered Deuteron Determination	53
5.6	Energy Loss in Target	56
6	Results and Error Analysis	61
6.1	Value of Effective Target Thickness	61
6.2	Error Analysis	64
7	Conclusion	65
A	Electrical Schematic Diagram	67

List of Figures

2-1	Flight paths at WNR. The neutron deuteron breakup experiment used flight path 4FP15R, marked ND Breakup. Detectors were located in building 29A [3].	18
2-2	False color image of the beam intensity profile. Produced by exposing a FUJI storage-phosphor image plate in the beam. The beam has a diameter of 1 in.	19
2-3	Experimental setup of detectors involved in measuring the position and energy of the scattered proton or neutron, to scale [7].	21
2-4	Experimental setup, to scale. Angles were calculated using the Law of Cosines.	23
3-1	Fission chamber uncalibrated ToF spectrum.	26
3-2	Time calibrator spectrum. The time calibrator output signals 10 ns apart, with a range of 1.28 μ s, which completely covers the range of the fission raw TOF spectrum. Only the part of the spectrum for which physical events occur during data collection is shown here.	27
3-3	Fission chamber ToF spectrum. The γ -flash is visible around 50 ns.	28
3-4	Fission chamber kinetic energy from ToF of the incident neutron. The maximum physical neutron kinetic energy for this experiment was 800 MeV.	29
3-5	Fission chamber ADC spectrum. The left peak corresponds to α -particles and the right peak to fission fragments. The minimum of the polynomial fit is channel 510.	29

3-6	The incident neutron kinetic energy as calculated by Equation 3.2 plotted against the fission chamber ADC.	30
3-7	^{238}U cross section spline	32
3-8	Incident neutron flux as determined by the yield of the fission chamber.	32
4-1	Incident neutron kinetic energy as a function of total time of flight, i.e. the time of flight of the incident neutron and elastically scattered deuteron. The thin black line is the spline fit, the black circles are the calculated values the spline is fit to.	37
4-2	Elastically scattered deuteron kinetic energy as a function of total time of flight, i.e. the time of flight of the incident neutron and elastically scattered deuteron. The thin black line is the spline fit, the blue circles are the calculated values the spline is fit to.	38
4-3	The red line is the energy of the incident neutron when energy lost by the elastically scattered deuteron in the liquid deuterium target is compensated for; the blue line is the energy of the incident neutron when the energy lost in the target is assumed to be zero. Note that for equal incident neutron energies, the spline fit which corrects for energy loss has longer total times of flight.	41
4-4	The blue line is the kinetic energy of the elastically scattered deuteron when energy lost by the deuteron in the liquid deuterium target is compensated for; the red line is the kinetic energy of the scattered deuteron when the energy lost in the target is assumed to be zero. Note that for equal deuteron energies, the spline fit which corrects for energy loss should have a shorter total time of flight, because higher energy neutrons produce higher energy deuterons. [Check This Tomorrow] .	41
5-1	The DE2 ADC value plotted against the CsI ADC value when the target is filled with liquid deuterium. Events outside the black graphical cut are considered to be from particles which are not deuterons. . . .	44
5-2	DE2 calibrated TOF, the γ -flash is visible around 60 ns.	45

5-3	CsI calibrated TOF, the smeared out $\gamma - flash$ is visible around 60 ns.	46
5-4	Incident neutron energy determined by total time of flight of the incident neutron and scattered deuteron as described in Section 4.4. . . .	46
5-5	DE2 vs CsI ADC spectra when the graphical deuteron cut in Figure 5-1 is applied for 6 different cuts on 10 MeV ranges of incident neutron kinetic energy are made.	47
5-6	DE2 ADC spectrum for liquid deuterium target after the graphical deuteron cut in Figure 5-1 is applied for 6 different cuts on 10 MeV ranges of incident neutron kinetic energy.	48
5-7	The CsI ADC spectrum shown for runs when the target was filled with liquid deuterium after the following cuts have been made: elastic trigger, deuteron graphical cut shown in Figure 5-1, an incident neutron in one of six different 10 MeV energy ranges, and the DE2 ADC cut described in Section 5.3.1.	50
5-8	The DE2 ADC value plotted against the CsI ADC value when the target is empty	52
5-9	DE2 vs CsI ADC spectra for empty target runs when the graphical deuteron cut in Figure 5-1 is applied for 6 different cuts on 10 MeV ranges of incident neutron kinetic energy are made.	53
5-10	The CsI ADC spectrum shown for runs when the target was empty after the following cuts have been made: elastic trigger, deuteron graphical cut shown in Figure 5-1, an incident neutron in one of six different 10 MeV energy ranges, and the DE2 ADC cut described in Section 5.3.1	54
5-11	Incident neutron energy determined by total time of flight of the incident neutron and scattered deuteron as described in Section 4.5. This accounts for energy lost by the elastically scattered deuteron in the liquid deuterium target.	56

5-12	DE2 vs CsI ADC spectra when the graphical deuteron cut in Figure 5-1 is applied for 6 different cuts on 10 MeV ranges of incident neutron kinetic energy are made (calculated with total time of flight of the neutron and scattered deuteron accounting for energy lost in the liquid deuterium target).	57
5-13	DE2 ADC spectrum for liquid deuterium target after the graphical deuteron cut in Figure 5-1 is applied for 6 different cuts on 10 MeV ranges of incident neutron kinetic energy (calculated with total time of flight of the neutron and scattered deuteron accounting for energy lost in the liquid deuterium target).	58
5-14	The CsI ADC spectrum shown for runs when the target was filled with liquid deuterium after the following cuts have been made: elastic trigger, deuteron graphical cut shown in Figure 5-1, an incident neutron in one of six different 10 MeV energy ranges (accounting for energy loss in the target), and the DE2 ADC.	59
A-1	Electrical schematic diagram for this experiment.	67

List of Tables

3.1	The dividing ADC cut between fission fragments and α -particles for different incident neutron energy ranges. The ADC cut for the energy range 0-800 MeV occurs at channel 510.	30
4.1	Elastic scattering cross section for neutron-deuteron scattering, found by interpolating data from telescopes located at angles of 36° and 42° presented in [4].	35
4.2	Bethe-Bloch variables.	38
5.1	DE2 ADC when the target is filled with liquid deuterium.	49
5.2	DE2 ADC cuts when the target is filled with liquid deuterium.	49
5.3	CsI ADC Gaussian fit parameters when the target is filled with liquid deuterium.	50
5.4	CsI ADC cuts when the target is filled with liquid deuterium.	51
5.5	Empty target events identified as deuterons.	53
5.6	Incident neutron flux and number of detected deuterons.	54
5.7	Alternative background determination for elastically scattered deuteron determination.	55
5.8	DE2 ADC when the target is filled with liquid deuterium and energy loss is accounted for when determining N_{inc} energy.	57
5.9	DE2 ADC cuts when the target is filled with liquid deuterium and energy loss is accounted for when determining N_{inc} energy.	58
5.10	CsI ADC Gaussian fit parameters when the target is filled with liquid deuterium and energy loss is accounted for when determining N_{inc} energy.	59

5.11	CsI ADC cuts when the target is filled with liquid deuterium and energy loss is accounted for when determining N_{inc} energy.	60
5.12	Incident neutron flux and number of detected deuterons.	60
6.1	Effective target thickness determined as described in Chapter 5. . . .	62
6.2	Mean and standard deviation of the values of the effective target thickness calculated for the 6 energy ranges shown in Table 6.1.	62

Chapter 1

Introduction

A great deal of experimental and theoretical work was devoted to understanding interactions between two nucleons (neutrons or protons). When the theoretical models of two nucleon interactions are extrapolated to interactions involving three nucleons, there are discrepancies between the theoretical predictions and the experimental results. This suggests the need for new theories to explain the physical process behind three nucleon interactions. This process is named the three nucleon force.

One of the simplest systems that involves the three nucleon force is considered to be a nucleon colliding with a bound neutron and proton (deuterium nucleus). The majority of such experiments involve a proton colliding with the deuterium nucleus, as in [8, 1, 9]. The experiment described in this thesis instead involves the collision of a neutron with a deuterium nucleus. The experiment seeks to measure the differential scattering cross section for interactions between the incident neutron and the bound proton over a wide range of incident neutron energies. The results in this experiment are the first that will measure this cross section for incident neutron kinetic energies above 25 MeV.

This thesis focuses on the determination of the yield of the incident neutron flux needed to measure the neutron induced deuteron breakup $d(n, np)n$ inelastic scattering cross section. The yield of the incident neutron flux depends on the total neutron flux and the effective thickness of the liquid deuterium target. The effective target thickness could potentially differ from the physical target thickness primarily

because of pressure induced bulging of the target container's windows and because of bubbling of the liquid deuterium. Pressure induced bulging increases the volume of the target, which increases the effective thickness relative to the physical thickness as measured at atmospheric pressure. The physical thickness of the target was measured when the target was at a pressure similar to the pressure maintained when the target was filled with liquid deuterium, but the target was not filled with liquid deuterium when this measurement was made. Bubbling of the liquid deuterium decreases the effective density of the deuterium, which decreases the effective thickness relative to the physical thickness. Bubbling of the liquid deuterium was qualitatively observed, but the quantitative effect that bubbling has on the liquid deuterium density was not directly measured.

A charged particle telescope, discussed in Section 2.5.3, was used to determine the effective target thickness by measuring the yield of deuterons elastically scattered by neutrons. This determination depends on several factors, which include: the incident neutron flux, discussed in Chapter 3, the solid angle of the detectors, discussed in Section 4.2, the live time of the detectors, discussed in Sections 3.4 and 4.3, and the detection of elastically scattered deuterons, discussed in Chapter 5. The analysis in this thesis determines the effective target thickness to be 2.0 ± 0.2 in, while the physical target thickness is thought to be no more than 1.2 in. This discrepancy suggests that at least one of the factors affecting the effective target thickness determination is not correctly accounted for, as discussed in Chapter 6.

Chapter 2

Experimental Setup

2.1 Overview of Experiment

The experiment was performed at the Weapons Neutron Research (WNR) facility at the Los Alamos Neutron Science Center (LANSCE) at the Los Alamos National Laboratory (LANL). At the WNR facility a beam of neutrons ranging in energy from a little above 0 MeV to 800 MeV was incident upon a liquid deuterium target. Two nucleons from the $d(n, np)n$ collision were observed in coincidence. The scattered proton was observed by a magnetic spectrometer on the right side of the beam (oriented in the direction the neutrons propagate), while one of the scattered neutrons was observed on the left side of the beam by a plastic scintillator.

2.2 Neutron Beam Production

The LANSCE linear accelerator accelerates protons up to 800 MeV before it directs them to a spallation tungsten source, called Target 4. The collision of the proton beam with Target 4 produces neutrons with energies ranging from below a few MeV to 800 MeV. The neutrons are collimated and directed down several beams into different experiments. This experiment used flight path 4FP15R, which is located 15° to the right of the proton beam when oriented in the direction in which the beam propagates. Figure 2-1 shows the different flight paths at WNR.

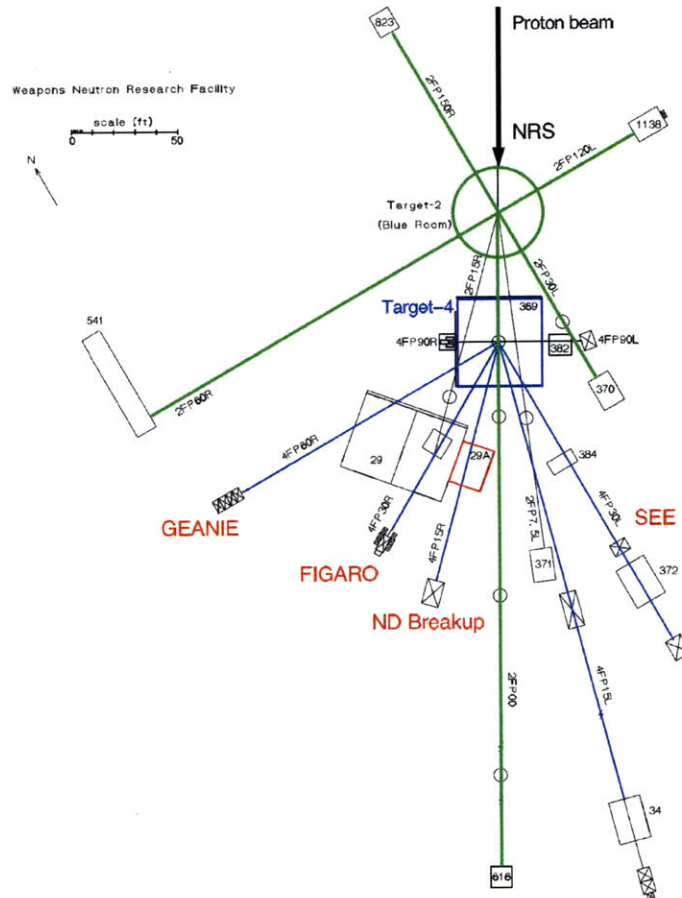


Figure 2-1: Flight paths at WNR. The neutron deuteron breakup experiment used flight path 4FP15R, marked ND Breakup. Detectors were located in building 29A [3].

As discussed in [4], the accelerator produces protons which collide with Target 4 to produce neutrons at a rate of 40 macropulses per second, with each macropulse having a width of $635 \mu s$. Each macropulse is made up of 0.2 ns long micropulses separated by $1.8 \mu s$. The short duration of each micropulse and long time between micropulses ensures that the slowest neutrons from one burst arrive before the fastest

neutrons from the next burst. The WNR facility provides each flight path with a signal that records the time at which the neutrons were produced, referred to in this thesis as t_0 .

The neutron beam to the flight path this experiment used is controlled by two depleted Uranium shutters. A shutter opening of 1.5 in x 1.5 in was used for this experiment. An iron collimator further reduced the size of the neutron beam. This collimator defined the final neutron beam size of a circle with a diameter of 1 in.

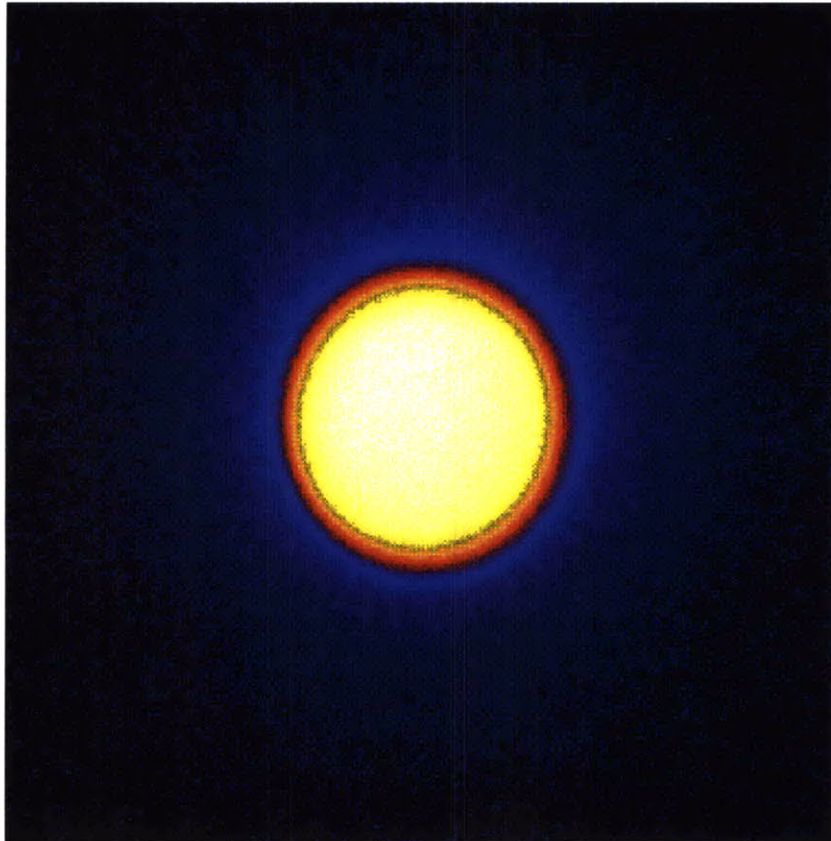


Figure 2-2: False color image of the beam intensity profile. Produced by exposing a FUJI storage-phosphor image plate in the beam. The beam has a diameter of 1 in.

2.3 Liquid Deuterium Target

A horizontal cylindrical flask, which measures 5 inches in diameter and 0.99 inches in thickness at atmospheric pressure, with 2 mil mylar windows served as the liquid deuterium target. This target could be filled with either liquid deuterium or liquid

hydrogen. In this experiment the fission chamber, discussed in Section 2.4, did not function properly when the target was filled with liquid hydrogen, which limits the usefulness of data collected during this time. The problem with the fission chamber was fixed before the target was filled with deuterium. The problem was fixed by placing 50 ohm BNC terminators on unused BNC connectors on the fission chamber to prevent charge buildup.

A cryogenic refrigeration system was used to cool the deuterium to a temperature of about 20 Kelvin and maintained a gauge pressure between 13.5 and 14 psi. At this pressure the target thickness was measured to be 1.1 in, but this measurement was made without liquid deuterium in the target. The liquid deuterium was observed to bubble at this pressure. The target was housed inside a large vacuum chamber. The chamber was shaped like a vertical cylinder with a diameter of 32 cm. The body of the vacuum chamber was made of $\frac{3}{16}$ inch stainless steel [4].

2.4 Fission Chamber

The flux of incident neutrons is determined using a fission ionization chamber, or fission chamber. The fission chamber was located 1545 cm downstream from Target 4, 145 cm upstream from the liquid deuterium target. The fission chamber contains several 0.0013 cm thick stainless steel foils which hold deposits of fissionable materials, such as ^{238}U . When neutrons pass through the fissionable material charged fission products, such as α -particles and heavy fission fragments are produced. The fission chamber outputs a signal which depends on the ionization caused by these charged fission products. The incident neutron flux was determined by measuring the yield of the neutron induced fission of ^{238}U , as described in Section 3.4.

2.5 Detectors

2.5.1 Proton Spectrometer

As discussed in Chapter 1 the goal of this experiment was to measure the quasielastic scattering cross section for neutron induced deuteron breakup, $d(n, np)n$. The scattered proton passed through a magnetic spectrometer as shown in Figure 2-3. Detectors DE1, P1 and P2 are made up of thin plastic scintillator material. Not shown in Figure 2-3 are two rear wire chambers, located between P1 or P2 and the rear magnet. These wire chambers are shown in Figure 2-4. These wire chambers can be used to determine the path the proton takes as it travels through the magnet spectrometer, and in theory can determine the energy of the proton through momentum resolution [3]. However, in practice it is difficult to get the position resolution of the wire chambers accurate and reliable enough to measure the proton momentum by how much it bends in the magnetic fields. The strength of each magnet is about 0.3 T.

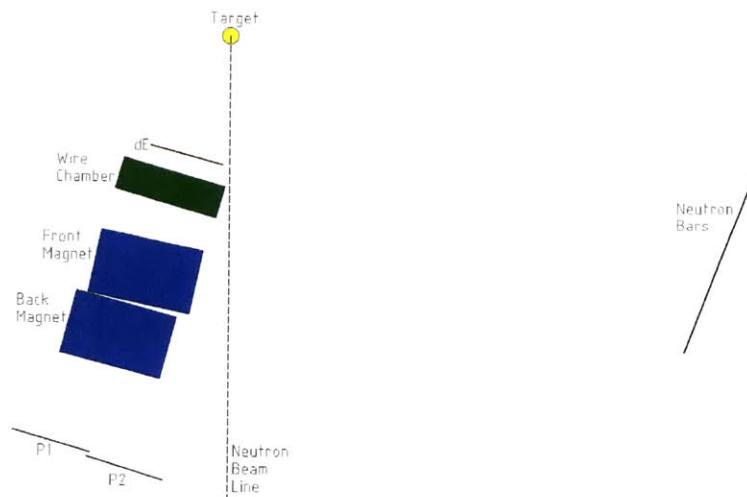


Figure 2-3: Experimental setup of detectors involved in measuring the position and energy of the scattered proton or neutron, to scale [7].

2.5.2 Neutron Detection

The position and time of flight of the scattered neutron was measured by one of nine plastic scintillators, labeled neutron bars in this experiment, positioned as shown in Figure 2-4. Although neutrons are not charged particles, they do scatter off the hydrogen and carbon nuclei in the scintillator. These scattered particles can be detected by the scintillator, with an efficiency of about 10% [4]. The energy of the scattered neutron was determined by measuring both the total time of flight of the incident and scattered neutron, as well as the total time of flight at two different positions of the incident neutron and scattered proton, as described in [7].

2.5.3 Charged Particle Telescope

This experiment used a charged particle telescope to measure the effective thickness of the target. The telescope consisted of a thin ΔE detector composed of plastic scintillator, labeled 'DE2' in this experiment, and a thick CsI calorimeter, composed of CsI crystal. The front center of the CsI calorimeter was located 203.9 cm from the center of the target at an angle of 40° to the left of the beam (oriented looking downstream). The center of the thin DE2 detector was located 203.7 cm from the center of the deuterium target, also at an angle of 40° to the left of the beam, as shown in Figure 2-4. The dimensions of the thin DE2 detector were 9.6 cm x 9.6 cm x 2.5 mm, while the dimensions of the thick CsI calorimeter in were 9.6 cm x 9.6 cm x 14 cm. The DE2 detector was positioned so as to completely cover the face of the CsI calorimeter.

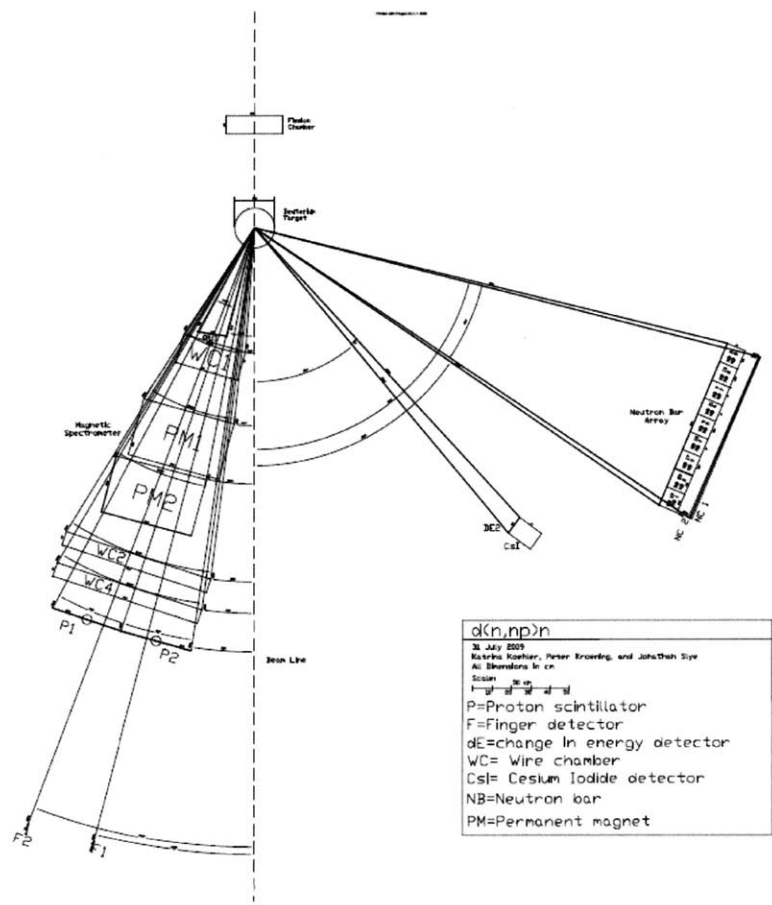


Figure 2-4: Experimental setup, to scale. Angles were calculated using the Law of Cosines.

Chapter 3

Incident Neutron Flux

3.1 Fission Chamber Overview

As discussed in Section 2.4, the flux of incident neutrons (N_{inc}) is determined by the fission chamber. The fission chamber outputs a signal proportional to the charge of the fission product produced by an incident neutron. This signal is recorded by an Analog to Digital Converter (ADC), and is used to distinguish between α -particles and heavier fission fragments, as discussed in Section 3.3. In addition, the time of flight of the neutron, or time difference between when the charged fission fragment was produced and the time when the neutron was produced at Target 4 was measured, as discussed in Section 3.2. The time of flight and ADC value determine the total flux of incident neutrons, as discussed in Section 3.4.

3.2 Fission Chamber Time of Flight

A Time to Amplitude Converter (TAC) was used to measure the time of flight of the incident neutron between Target 4 and the fission chamber. The output pulse from the fission chamber was sent to a Constant Fraction Discriminator (CFD), the CFD output a logic signal that was the start signal of the TAC. The stop signal of the TAC was a delayed t_0 pulse (described in Section 2.2). The TAC output signal was recorded by an ADC.

The spectrum of the ADC for about 200 hours of data collection is shown in Figure 3-1. During this series of runs the amount that the t_0 signal was delayed before stopping the TAC did not change by more than about 1 ns. During the experiment t_0 was observed to change suddenly, within the course of a single 2 hour run, relative to the experiment several times; this drift in t_0 was corrected for by adding a run dependent offset when calibrating the detectors. The cause of t_0 drift was either drift in the t_0 pulse sent to all experiments, often after a period of time when the beam was off, or a change in this experiment's setup.

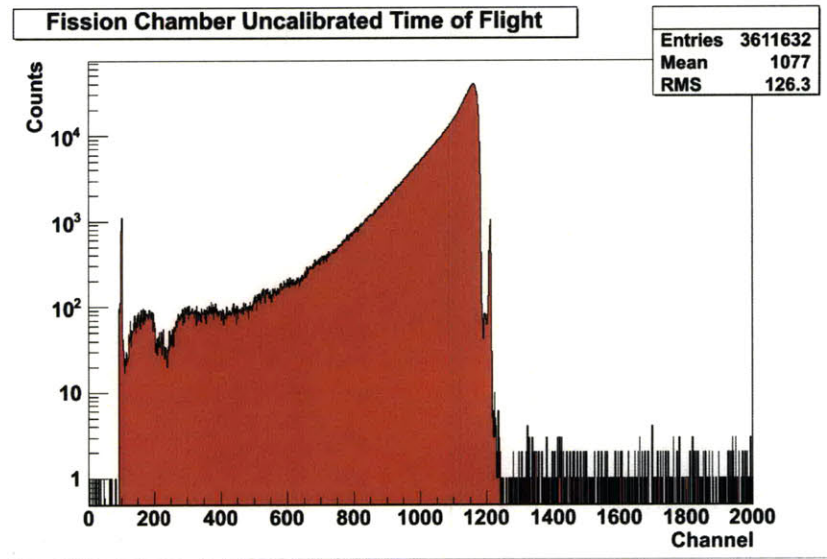


Figure 3-1: Fission chamber uncalibrated ToF spectrum.

The fission chamber ToF spectrum was calibrated using a time calibrator and an event with a known time of flight. The time calibrator also tested the linearity of the ADC. Figure 3-2 shows that the ADC is linear. The straight line fit has a reduced χ^2 of 0.29 assuming an error of 1 channel. This calibration gives a conversion factor of $0.3625ns \cdot chn^{-1}$. When the proton beam is incident upon Target 4, a prompt γ emission occurs. The emitted γ -rays travel at the speed of light. This is referred to as the γ -flash and is important for calibrating many detectors in this experiment. The γ -flash is visible around channel 1210 in Figure 3-1. The γ -flash travels the 1545 cm between Target 4 and the fission chamber in 51.5 ns.

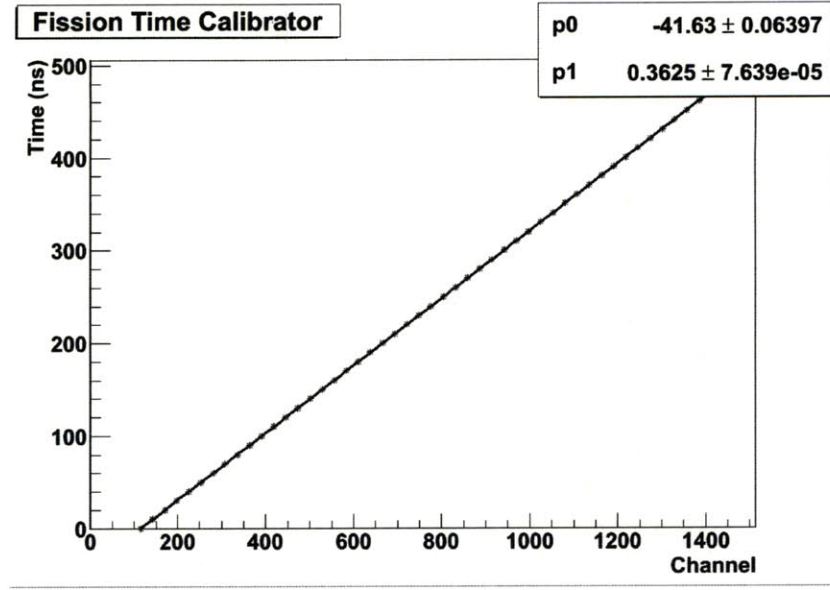


Figure 3-2: Time calibrator spectrum. The time calibrator output signals 10 ns apart, with a range of $1.28 \mu s$, which completely covers the range of the fission raw TOF spectrum. Only the part of the spectrum for which physical events occur during data collection is shown here.

The final conversion from channels to ns is given by Equation 3.1.

$$TOF_{cal} = a - (b \cdot TOF_{raw}) \quad (3.1)$$

where a is the time offset, 488.9 ns for this set of runs, and $b = 0.3625 \text{ ns} \cdot \text{ch}^{-1}$ was calculated using the time calibrator, TOF_{cal} is the time of flight in ns, while TOF_{raw} is the time of flight in channels. For different sets of runs the value of a was adjusted to correct for drift over time in t_0 relative to the fission chamber signal. The upper bound on the error associated with the fission chamber timing can be estimated by the width of a Gaussian fit around the γ -flash. The standard deviation, σ , of this Gaussian fit was .7 ns. The calibrated ToF spectrum of the fission chamber is shown in Figure 3-3.

3.2.1 Incident Neutron Kinetic Energy

The ToF was converted into an energy spectrum through standard relativistic kinematics, as shown in Equation 3.2.

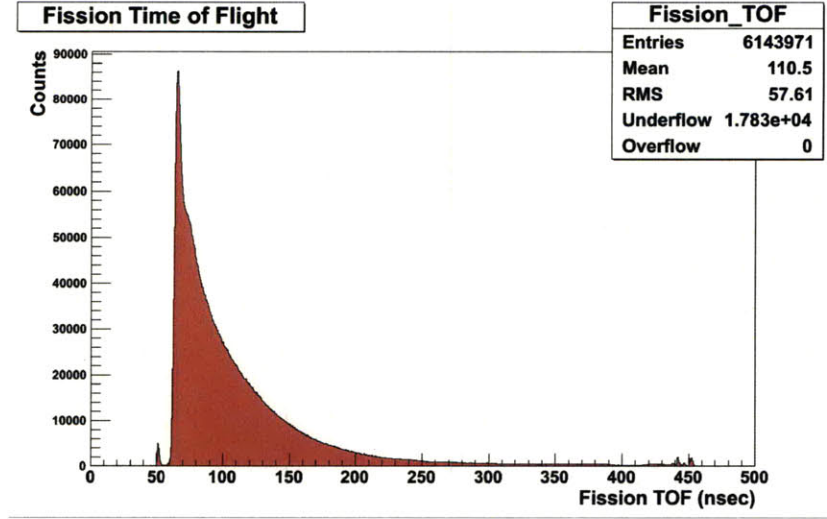


Figure 3-3: Fission chamber ToF spectrum. The γ -flash is visible around 50 ns.

$$T = \frac{mc^2}{\sqrt{1 - v^2/c^2}} - mc^2 \quad (3.2)$$

where T is the kinetic energy of the incident neutron in MeV, mc^2 is the neutron mass in MeV, and v is the velocity of the neutron and c is the speed of light.

The resulting spectrum is shown in Figure 3-4. This is similar to the spectrum obtained in past experiments using a similar setup [7, 4, 2].

3.3 Fission Chamber ADC Spectrum

The amplitude of the fission chamber output signal was recorded by an ADC. This ADC value was used to distinguish between α -particles and charged fission fragments. α -particles are produced both by α -decay of the ^{238}U and by collisions between the neutrons from the beam and the stainless steel foil in the fission chamber [4]. The fission fragments produce larger signals than the α -particles do, so the fission fragments produce higher ADC values than the α -particles do. A quadratic polynomial was fit to the dip in the ADC between α -particle and fission fragments. The minimum value of this polynomial was used to discriminate against α -particles, as shown in Figure 3-5.

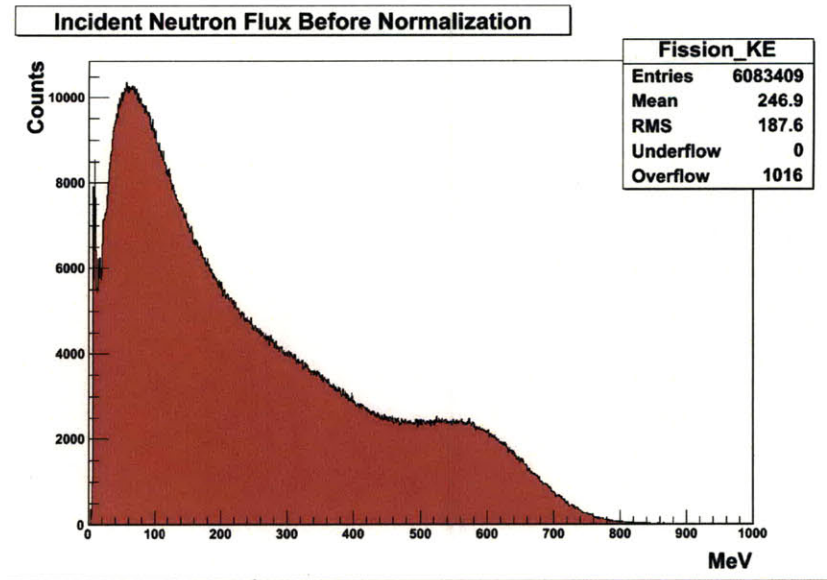


Figure 3-4: Fission chamber kinetic energy from ToF of the incident neutron. The maximum physical neutron kinetic energy for this experiment was 800 MeV.

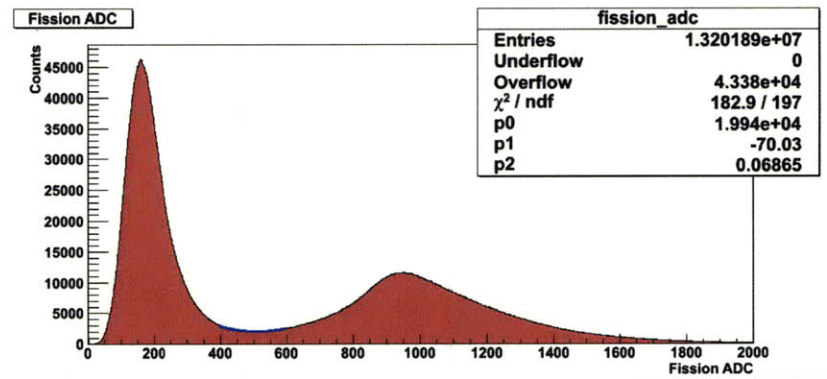


Figure 3-5: Fission chamber ADC spectrum. The left peak corresponds to α -particles and the right peak to fission fragments. The minimum of the polynomial fit is channel 510.

The number of α -particles produced relative to the number of heavy fission fragments produced changes as a function of incident neutron energy. Therefore it is possible that the position of the ADC minimum changes as a function of incident neutron energy. Figure 3-6 shows how the fission chamber ADC spectrum varies with incident neutron kinetic energy.

In the analysis a different value of the ADC cut of α -particles was used for different energy ranges. The analysis in this thesis focuses on six different energy ranges,

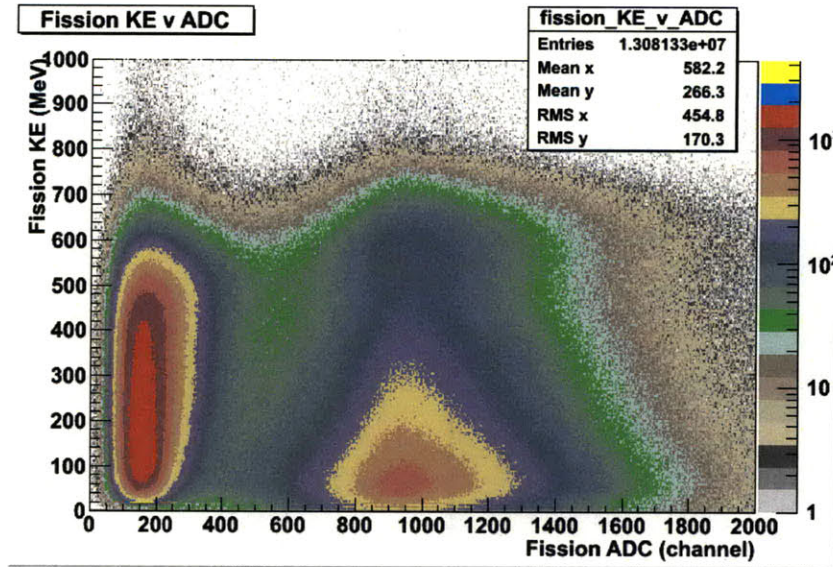


Figure 3-6: The incident neutron kinetic energy as calculated by Equation 3.2 plotted against the fission chamber ADC.

as discussed in Section 4.2. The minimum values of the ADC which was considered a fission fragment for these energy ranges are displayed in Table 3.1. Higher energy ranges tend to have a higher ADC cutoff value, which qualitatively agrees with Figure 3-6.

Table 3.1: The dividing ADC cut between fission fragments and α -particles for different incident neutron energy ranges. The ADC cut for the energy range 0-800 MeV occurs at channel 510.

Incident Neutron Kinetic Energy [MeV]	Minimum ADC Value Not Considered an α -particle [chn]
135 – 145	471.7
155 – 165	479.6
175 – 185	489.7
195 – 205	506.5
215 – 225	528.6
235 – 245	536.1

3.4 Incident Neutron Flux

The flux of incident neutrons (N_{inc}), is related to the number of neutrons detected by the fission chamber by Equation 3.3.

$$N_{inc}(E) = \frac{N_{fis}(E)}{\epsilon l_{fis} \rho_U \sigma_U(E)} \quad (3.3)$$

where $N_{inc}(E)$ is the incident neutron flux as a function of incident neutron kinetic energy, N_{fis} is the number of neutrons detected by the fission chamber, ϵ is the efficiency of the fission chamber, l_{fis} is the live time of the fission chamber, ρ_U is the density of ^{238}U in the fission chamber and $\sigma_U(E)$ is the cross section for fission fragments to be produced for incident neutrons with a kinetic energy E . The live time of the fission chamber, l_{fis} , can be measured with the help of a scaler, but this analysis has yet to be done. It is believed that the live time should be very close to 1 because the count rate of the fission chamber is low (about 6 Hz), and the electronics associated with the fission chamber are decoupled from the other detectors in the experiment. From [11], ϵ is 0.98 and ρ_U is $0.9080 \cdot 10^{-6}$ atoms·barn⁻¹. The cross section of ^{238}U as a function of energy is determined by fitting a spline to interpolate and extrapolate between the known data points. The spline fit is shown in Figure 3-7. As discussed in [2], there is not much data for neutrons with kinetic energies above about 100 MeV, which introduces an error of about 10% on the spline.

Equation 3.3 is used to determine to the total flux of neutrons, shown in Figure 3-8. An ADC cut above channel 510 was applied to select out fission fragments when making the histogram shown in Figure 3-8.

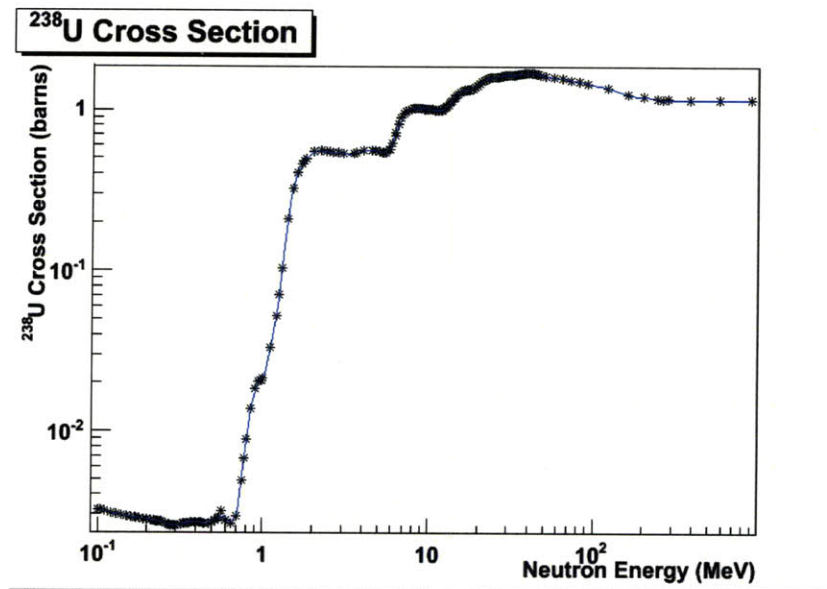


Figure 3-7: ²³⁸U cross section spline

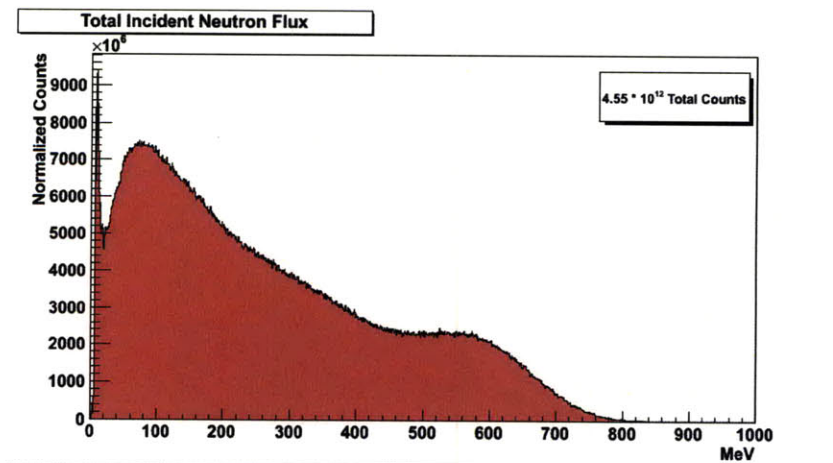


Figure 3-8: Incident neutron flux as determined by the yield of the fission chamber.

Chapter 4

Effective Target Thickness

4.1 Principles of Effective Target Thickness

The effective target thickness, x_{eff} , is the length that a neutron from the beam would travel as it passed through the target if the neutron did not interact with any of the matter inside the target. While the physical target thickness, x_{phy} , was measured to be 1.1 inches when at a gauge pressure of 14 psi, the x_{eff} could differ from this measurement, as discussed in Chapter 1. The measurement of x_{phy} could be different for the liquid deuterium target because it was not made when the target was filled with liquid deuterium. Additionally, the liquid deuterium bubbled, which decreases its density, ρ . While this bubbling affects ρ and not the x_{eff} , in this thesis this effect is accounted for by changing x_{eff} and keeping ρ constant. If x_{eff} determined in this thesis is used in the determination of the quasielastic scattering cross section for the $d(n, np)n$ interaction, as discussed in [10], the expression used would be $x_{eff} \cdot \rho$. There is no need in this thesis to separately define an effective target thickness and an effective target density; instead any factor which would change ρ is accounted for by its effect on the determination of x_{eff} . Finally the target could be oriented at a small angle to the beam, which would increase x_{eff} relative to x_{phy} by a factor of $1/\cos\theta$, where θ is the angle of the liquid deuterium target relative to the beam.

4.2 Effective Target Thickness

The effective target thickness, x_{eff} is determined by measuring the yield of elastic scattering between deuterons and neutrons from a liquid deuterium target, as given by Equation 4.1.

$$x_{eff} = \frac{N_d}{\epsilon_d N_{inc}} \cdot \frac{k}{\Delta\Omega_d \rho l} \cdot \frac{1}{\frac{d\sigma}{d\Omega_d}} \quad (4.1)$$

where x_{eff} is the effective thickness in cm, N_d is the number of detected deuterons which are elastically scattered into $\Delta\Omega_d$, the solid angle of the charged particle telescope given by Equation 4.3, N_{inc} is the flux of incident neutrons discussed in Section 3.4, k is the electronic prescale factor (which is set to 1), ρ is the density of the liquid deuterium ($5.1 \cdot 10^{-5}$ atoms \cdot mb $^{-1}\cdot$ cm $^{-1}$) as given by Equation 4.2, l is the live time of the DE2 - CsI detectors discussed in Section 4.3, and $\frac{d\sigma}{d\Omega_d}$ is the neutron-deuteron elastic scattering cross section, determined in [4], and shown in Table 4.1. Note that while x_{eff} should be independent of the energy of the incident neutron, N_d , N_{inc} and $\frac{d\sigma}{d\Omega_d}$ all depend on the incident neutron energy. The calculation of the cross section is performed for 6 different neutron energy ranges; the standard deviation of x_{eff} determined at these 6 energies is related to the error associated with this determination.

The density of the liquid deuterium in the target is given by Equation 4.2.

$$\rho = \rho_{g/cm^3} \frac{N_A}{A_{D_2}} \cdot 10^{-27} \quad (4.2)$$

where ρ is the density of liquid deuterium in the target in atoms \cdot mb $^{-1}\cdot$ cm $^{-1}$, ρ_{g/cm^3} is the density of liquid deuterium in grams per centimeter cubed, 0.169 g \cdot cm $^{-3}$ for a gauge pressure of 14 psi as given by [4], N_A is Avogadro's number ($6.022 \cdot 10^{23}$ atoms \cdot mol $^{-1}$), and A_{D_2} is the molar mass of deuterium (2.014 g \cdot mol $^{-1}$).

The solid angle occupied by the charged particle telescope is given by:

$$\Delta\Omega_d = \frac{A_{tel}}{x_{tel}^2} \quad (4.3)$$

where $\Delta\Omega_d$ is the solid angle of the telescope (0.0022 sr), A_{tel} is the area of the charged particle telescope normal to the elastically scattered deuterons (which is 9.6 cm x 9.6 cm as discussed in Section 2.5.3, thus $A_{tel} = 92.16\text{cm}^2$, and x_{tel} is the distance from the center of the target to the center of the telescope (203.7 cm).

Table 4.1: Elastic scattering cross section for neutron-deuteron scattering, found by interpolating data from telescopes located at angles of 36° and 42° presented in [4].

Neutron Energy [MeV]	$\frac{d\sigma}{d\Omega_d}$ [mb·sr ⁻¹]	Error of $\frac{d\sigma}{d\Omega_d}$ [mb·sr ⁻¹]
140	0.285	0.028
160	0.211	0.021
180	0.136	0.014
200	0.11	0.011
220	0.091	0.009
240	0.085	0.006

4.3 Live Time of the Data Acquisition System

The live time of the data acquisition system (DAQ) is given by the fraction of detected deuterons that are read by the computer and stored as data. It could be determined with the help of a scaler, as given by Equation 4.4.

$$l = \frac{N_{comp}}{N_{scal}} \quad (4.4)$$

where l is the live time, N_{scal} is the number of triggers recorded by a scaler, and N_{comp} is the number of triggers recorded by the computer. Unfortunately, there was no scaler which counted the number of charged particle telescope triggers (called elastic triggers in this thesis). However, the live time of the charged particle telescope is dominated by the live times associated with the DAQ, which could be determined with the help of scalers. The live time was assumed to be unity in this thesis; further analysis will be performed to check the validity of this assumption.

4.4 Kinetic Energy of Incident Neutron and Elastically Scattered Deuteron from the ToF of the Neutron and Deuteron

The thin DE2 plastic scintillator, discussed in Section 2.5.3, provides good timing resolution, a minimum resolution of 0.4 ns as discussed in Section 5.2, for determining the total time of flight, i.e. the time of flight of the incident neutron and the scattered deuteron. This one quantity is sufficient to define both the kinetic energy of the incident neutron and the kinetic energy of the scattered deuteron. However, it is nontrivial to solve these equations algebraically, so a numerical solution was constructed. This numerical solution can be arbitrarily precise, so it adds negligible error over the algebraic solution.

From relativistic kinematics [5],

$$\cos \theta_r = \frac{(E_n + m_n c^2 + m_d c^2) E_d}{\sqrt{E_n (E_n + 2m_n c^2) E_d (E_d + 2m_n c^2)}} \quad (4.5)$$

where θ_r is the angle of the scattered deuteron in the lab frame (40°), E_n is the kinetic energy of the incident neutron [MeV], $m_n c^2$ is the neutron rest mass (939.57 MeV), E_d is the energy of the scattered deuteron [MeV], $m_d c^2$ is the deuteron rest mass (1877.84 MeV) and c is the speed of light ($29.98 \text{ cm}\cdot\text{ns}^{-1}$). This equation is then solved for E_d as a function of E_n :

$$E_d = \frac{(\cos \theta_r)^2 E_n (E_n + 2m_n c^2) 2m_n c^2}{(E_n + m_n c^2 + m_d c^2)^2 - (\cos \theta_r)^2 E_n ((E_n + 2m_n c^2))} \quad (4.6)$$

where all variables are the same as in Equation 4.5.

Now the total time of flight, t_{tot} is related to E_d and E_n by

$$t_{tot} = \frac{x_n}{\beta_n c} + \frac{x_{tel}}{\beta_d c} \quad (4.7)$$

where x_n is the distance traveled by the neutron to the target (1693.0 cm), x_{tel} is

the distance from the center of the liquid deuterium target to the center of the DE2 scintillator (203.7 cm), and $\beta = \sqrt{1 - \frac{(mc^2)^2}{(E+mc^2)^2}}$ with β , E and m being replaced by β_n , E_n , m_n for the incident neutron and β_d , E_d , m_d for the elastically scattered deuteron.

These equations were solved numerically. The spline fits of the numerical solution are shown in Figure 4-1 and Figure 4-2.

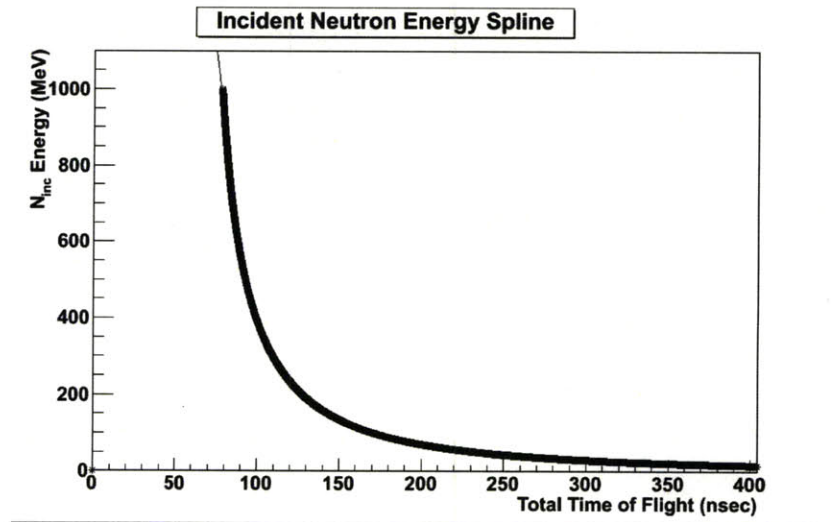


Figure 4-1: Incident neutron kinetic energy as a function of total time of flight, i.e. the time of flight of the incident neutron and elastically scattered deuteron. The thin black line is the spline fit, the black circles are the calculated values the spline is fit to.

4.5 Energy Loss in Target

Deuterons are charged particles which lose energy when passing through matter. Although deuterons lose energy in all stages of the flight from inside the target to the DE2 detector, as described in [4], only the loss of energy while in the liquid deuterium target will be discussed here. Energy lost in the target is likely to be the most significant in affecting the time of flight of the deuteron because energy lost in the target will affect the entire flight path of the deuteron, while energy lost in latter stages of the flight (for instance in the thin DE2 scintillator which is only 2 mm from the CsI detector) will have a smaller effect on the deuteron time of flight.

Because the deuterons move at relativistic velocities ($\beta_d = 0.23$ for $E_d = 51.8$ MeV;

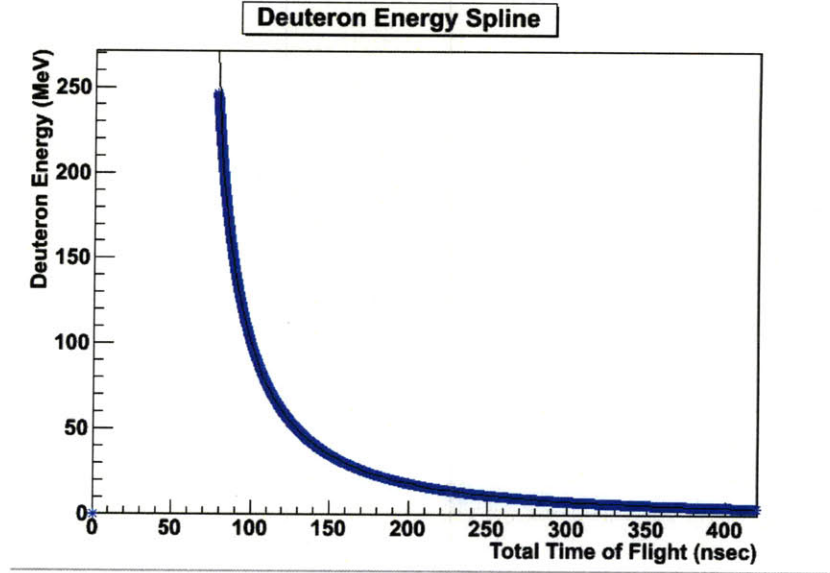


Figure 4-2: Elastically scattered deuteron kinetic energy as a function of total time of flight, i.e. the time of flight of the incident neutron and elastically scattered deuteron. The thin black line is the spline fit, the blue circles are the calculated values the spline is fit to.

which are produced when $E_n = 200$ MeV), the Bethe-Bloch formula as discussed in [6] is used. On the other hand, the energy of the scattered deuteron is small enough such that the density effect and shell correction are negligible.

$$-\frac{dE}{dx} = 2\pi N_a (r_e)^2 m_e c^2 \rho \frac{Z}{A} \frac{z^2}{\beta^2} \left[\ln\left(\frac{2m_e \gamma^2 v^2 T_{max}}{I^2}\right) - 2\beta^2 \right] \quad (4.8)$$

with $2\pi N_a (r_e)^2 m_e c^2 = 0.1535 \text{ MeV} \cdot \text{cm}^2 \cdot \text{g}^{-1}$.

Table 4.2: Bethe-Bloch variables.

r_e	$2.817 \cdot 10^{-13}$ cm electron radius	ρ	density of absorber
T_{max}	max energy transfer in one collision	m_e	electron mass
N_a	Avogadro's number $6.022 \cdot 10^{23}$ atoms/mol	β	v/c
I	mean excitation potential	z	charge in units of e
A	atomic weight of absorbing material	Z	atomic number

For the liquid deuterium target: $\rho = (0.169 \text{ g} \cdot \text{cm}^{-3})$, $z = 1$ electron, $A = 2.014 \text{ g} \cdot \text{mol}^{-1}$, I is assumed to be the same as for liquid hydrogen (19.6 eV), $Z = 1$, and because $m_d \gg m_e$ T_{max} is given by Equation 4.9.

$$T_{max} = 2m_e c^2 \beta^2 \gamma^2 \quad (4.9)$$

where $\gamma = 1/\sqrt{1 - \beta^2}$, and $m_e c^2$ is the electron mass in MeV. Using these numbers, a 50 MeV deuteron (about a 200 MeV incident neutron) loses 3.9 MeV per cm or has $-\frac{dE}{dx} = 3.9 \text{ MeV}\cdot\text{cm}^{-1}$ in the liquid deuterium target.

These equations were used to modify the kinematics discussed in Section 4.4.

$$E'_d = E_d - E_{loss} \quad (4.10)$$

where E'_d is the energy of the elastically scattered deuteron after it leaves the target, E_d is defined in Equation 4.6, and E_{loss} is the energy lost in the target, defined in Equation 4.11.

The energy lost in the target is calculated with the simplifying assumption that the loss of energy is small enough that it is constant across the length of the target. A 50 MeV deuteron loses about 4 MeV per cm, therefore this assumption is justifiable for the deuterons produced by incident neutrons with kinetic energy in the energy ranges used in the analysis presented in this thesis.

$$E_{loss} = \int -\frac{dE_d}{dx} dx \approx -\frac{dE_d}{dx} \Delta x \quad (4.11)$$

where Δx is the length of the path the deuteron travels in the liquid deuterium target and $-\frac{dE}{dx}$ is given by Equation 4.8. Assuming the neutron-deuteron occurs at the center of the target (and that the height of the center of the charged particle telescope is the same height as the target),

$$\Delta x = .5x_{eff} / \cos(\theta_{tel}) \quad (4.12)$$

where x_{eff} is the effective thickness of the target, and $\cos(\theta_{tel})$ is the angle at which the charged particle telescope is located relative to the beam. Approximating x_{eff} as the physical target thickness $x_{phy} = 2.8 \text{ cm}$, the average Δx is 1.8 cm. Note that the variable x_{eff} which is being determined is used to calculate the energy loss in

the target; this suggests the best way to analyze this data is in an iterative manner. Due to time constraints this analysis was not performed; however incorporating the energy lost in the target has a relatively small effect, about a 10% increase in x_{eff} , so as long as x_{eff} does not differ too much from x_{phy} the iterative process will not lead to too large a difference. The analysis found that x_{phy} and x_{eff} did differ by a large factor ($x_{eff} \approx 1.8x_{phy}$), but this means that x_{eff} was unphysically large, and adding energy loss would make it even larger. So there are larger errors somewhere in either the analysis or the experimental setup than the error caused by not iterating the process. Using x_{phy} for x_{eff} , a 50 MeV deuteron loses about 7 MeV in the target. This is a little less than the result found in [4] which uses a similar setup, but gives the energy loss for the entire flight path of the deuteron as about 10 to 15 MeV for deuterons scattered into a telescope located at an angle of 24° relative to the neutron beam.

Equation 4.7 is modified to use E'_d as opposed to E_d . A spline interpolation is shown in Figure 4-3 relating the total time of flight to the energy of the incident neutron, and a spline interpolation relating the total time of flight to the energy of the scattered deuteron is shown in Figure 4-4.

Not accounting for the energy loss in the target tends to cause an underestimation of the effective target thickness, x_{eff} , as defined by Equation 4.1. The neutron-deuteron scattering cross section $\frac{d\sigma}{d\Omega_d}$ given in Table 4.5, and the incident neutron flux, N_{inc} , shown in Figure 3-8, both increase as incident neutron kinetic energy decreases. The effective target thickness x_{eff} varies inversely with the product $N_{inc} \cdot \frac{d\sigma}{d\Omega_d}$, thus as the incident neutron kinetic energy decreases, so does x_{eff} if all else (specifically the number of elastically scattered deuterons) is constant. An underestimation of the incident neutron kinetic energy leads to an underestimation of x_{eff} . As shown in Figure 4-3, not accounting for energy loss in the target leads to an underestimation of the incident neutron kinetic energy, therefore it leads to an underestimation of x_{eff} . This is shown in Chapter 6.

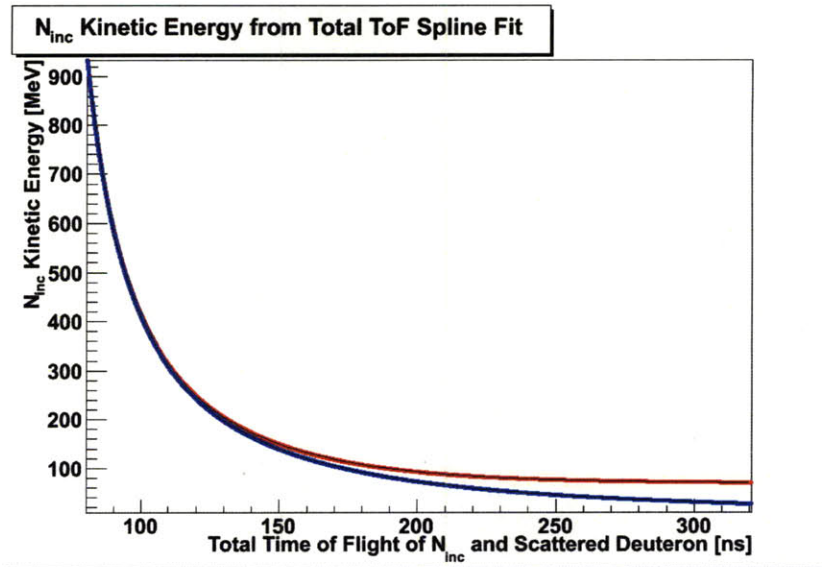


Figure 4-3: The red line is the energy of the incident neutron when energy lost by the elastically scattered deuteron in the liquid deuterium target is compensated for; the blue line is the energy of the incident neutron when the energy lost in the target is assumed to be zero. Note that for equal incident neutron energies, the spline fit which corrects for energy loss has longer total times of flight.

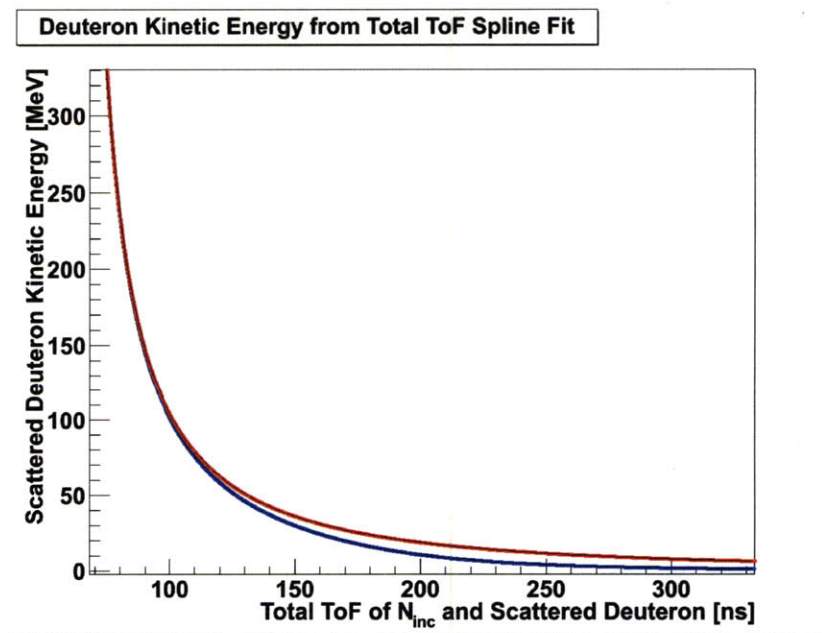


Figure 4-4: The blue line is the kinetic energy of the elastically scattered deuteron when energy lost by the deuteron in the liquid deuterium target is compensated for; the red line is the kinetic energy of the scattered deuteron when the energy lost in the target is assumed to be zero. Note that for equal deuteron energies, the spline fit which corrects for energy loss should have a shorter total time of flight, because higher energy neutrons produce higher energy deuterons. [Check This Tomorrow]

Chapter 5

Measurement of Elastically Scattered Deuteron

5.1 Identification of Elastically Scattered Deuteron

The charged particle telescope described in Section 2.5.3 can be used to distinguish between elastically scattered deuterons and quasielastically scattered protons. The CsI calorimeter is thick enough to completely stop the deuteron or proton; thus its output signal depends on the kinetic energy of the particle. The DE2 (ΔE) thin plastic scintillator does not stop charged particles with energies of our concern; it outputs a signal which depends on both the particle's kinetic energy and velocity. Because a deuteron has a mass about twice that of a proton, a deuteron with the same kinetic energy as a proton will deposit more energy in the DE2 detector than the proton will. The CsI detector depends on the kinetic energy, mass and charge of the particle in a different manner than the DE2 detector does. Deuterons can be identified by comparing the DE2 output signal to the CsI output signal. The CsI output signal and the DE2 output signal are recorded by separate ADCs. This is shown in Figure 5-1.

For runs in which the target was filled with liquid deuterium, there were $9.35 \cdot 10^7$ triggers recorded in this experiment. The majority of these triggers were used to determine the quasielastic $d(n, np)n$ scattering cross section. Only the charged

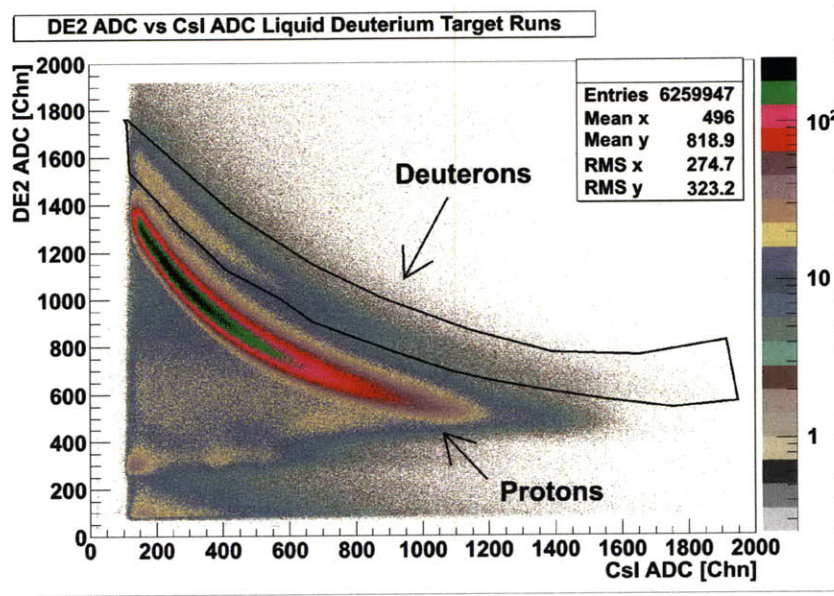


Figure 5-1: The DE2 ADC value plotted against the CsI ADC value when the target is filled with liquid deuterium. Events outside the black graphical cut are considered to be from particles which are not deuterons.

particle telescope (or elastic) trigger, which required a t_0 pulse and a coincidence between the CsI and DE2 detectors, was used for the determination of the number of scattered deuterons. There were $6.26 \cdot 10^6$ elastic triggers. Of the elastic triggers $4.65 \cdot 10^5$ were caused events in the graphical deuteron cut shown in Figure 5-1.

5.2 Total Time of Flight of the Neutron and Elastically Scattered

The total time of flight of the incident neutron and elastically scattered deuteron determines the energy of the incident neutron and scattered deuteron as described in Section 4.4. The total time of flight is determined with the help of two TDCs. The start signal of the first TDC is the elastic trigger. The output signal of the DE2 detector is sent to a CFD, which outputs a logic signal that serves as the stop signal of the first TDC. Additionally, the t_0 signal is recorded by the second TDC. This t_0 is subtracted from the value of the first TDC to determine the total time of flight of the neutron and deuteron. Because the DE2 detector is made of plastic scintillator

while the CsI detector is a CsI crystal, the DE2 detector has better timing resolution than the CsI detector. The timing resolution is estimated by taking the standard deviation of a Gaussian fit to the γ -flash. The γ -flash is discussed in Section 3.2. The DE2 Gaussian fit has a standard deviation of 0.4 ns, which serves as an estimate of the minimum timing resolution of the detector. The DE2 detector was calibrated using a time calibrator and γ -flash identification. The γ -flash arrives at the DE2 detector 63.3 ns after the proton beam collides with Target 4. The calibrated DE2 ToF spectrum is shown in Figure 5-2.

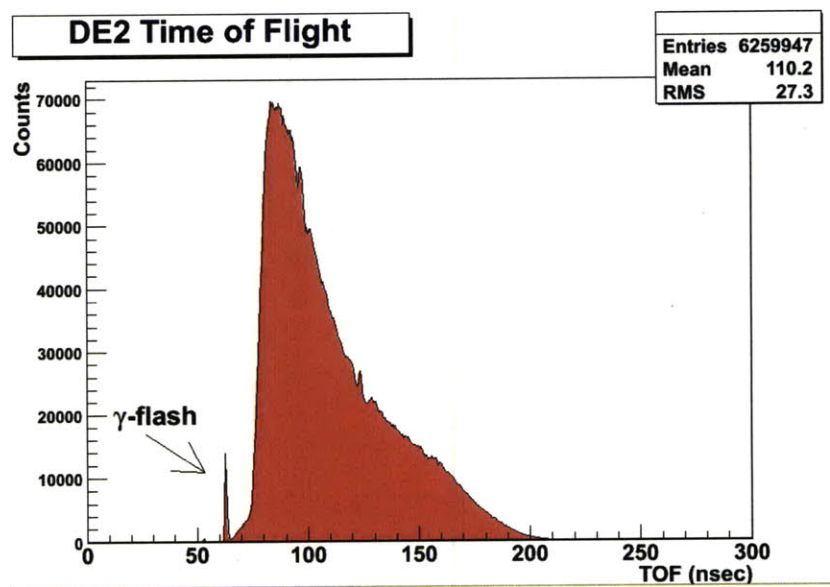


Figure 5-2: DE2 calibrated TOF, the γ -flash is visible around 60 ns.

Because the CsI detector has worse timing resolution than the DE2 detector, its time of flight spectrum was not used in the analysis. However, it should look qualitatively similar to the time of flight spectrum of the DE2 detector. The CsI was calibrated in the same manner as the DE2 detector was. Note that the γ -flash is smeared out, as shown in Figure 5-3.

The total time of flight of the incident neutron and elastically scattered deuteron as determined by the DE2 detector was converted into an incident neutron energy spectrum, shown in Figure 5-4, as described in Section 4.4. This spectrum has a different shape than the incident neutron energy spectrum derived from the fission chamber, shown in Figure 3-4. One possible explanation for this is that the cross

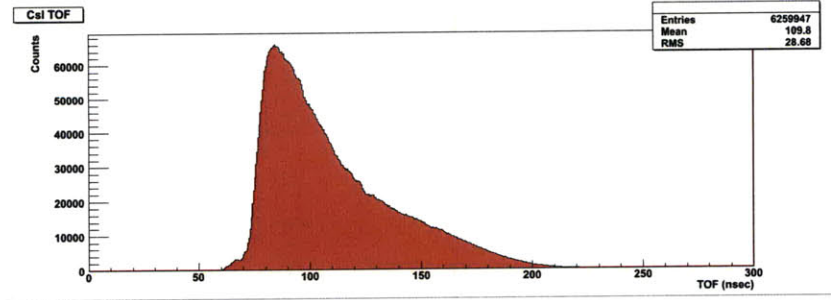


Figure 5-3: CsI calibrated TOF, the smeared out γ - flash is visible around 60 ns.

section for neutron-deuteron scattering differs from the cross-section for neutron induced fission. Another possibility is that low energy neutrons scatter deuterons which do not have enough energy to escape from the target. Finally, Figure 5-4 does not account for energy loss of the elastically scattered deuteron in the liquid deuterium target; this loss is accounted for in Figure 5-11.

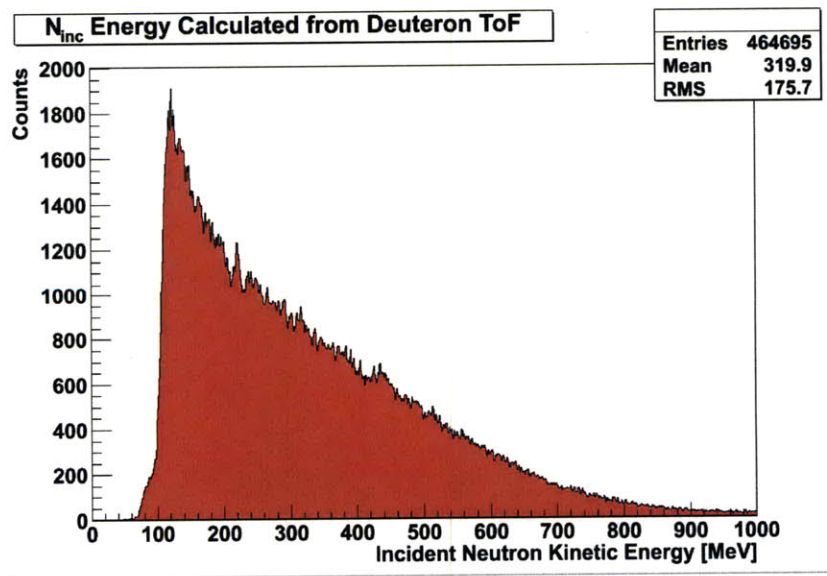


Figure 5-4: Incident neutron energy determined by total time of flight of the incident neutron and scattered deuteron as described in Section 4.4.

5.3 Number of Detected Deuterons as a Function of Incident Neutron Energy

The effective target thickness, x_{eff} , should be independent of the energy of the incident neutron, thus measuring it for a few different incident neutron kinetic energy ranges serves both to increase the statistics and as a test of the error associated with the measurement. The incident neutron kinetic energy ranges used, in MeV, were 140 ± 5 , 160 ± 5 , 180 ± 5 , 200 ± 5 , 220 ± 5 and 240 ± 5 . These energy ranges were chosen because the neutron deuteron elastic scattering cross section is well known at these energies for similar angles of scattering to the angle of scattering used in this experiment (40° in the lab frame) [4].

The energy of the incident neutron is determined by the total time of flight of the neutron and elastically scattered deuteron, as described in Section 5.2. When an incident neutron energy cut is made it selects out a small region of the deuterons shown in Figure 5-1. This is shown in Figure 5-5.

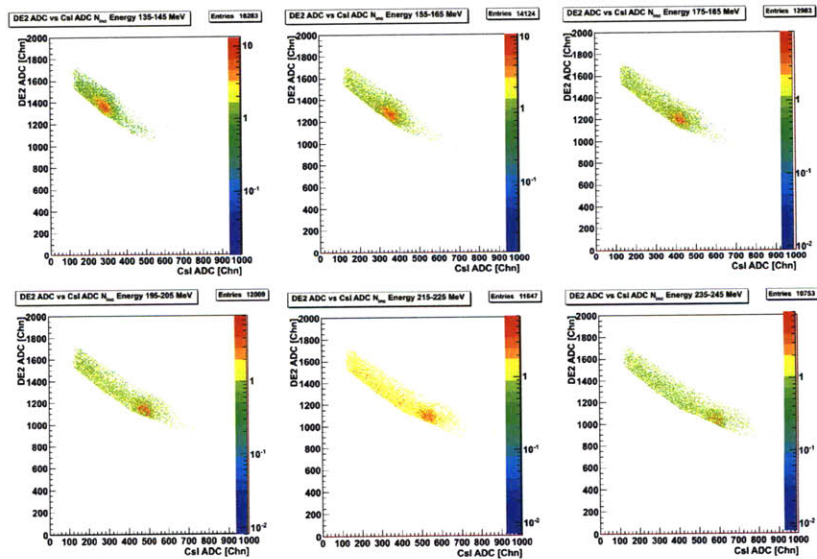


Figure 5-5: DE2 vs CsI ADC spectra when the graphical deuteron cut in Figure 5-1 is applied for 6 different cuts on 10 MeV ranges of incident neutron kinetic energy are made.

5.3.1 DE2 ADC Cut for Elastically Scattered Deuterons

A two step process was applied for each energy range to select out the scattered deuterons. First a Gaussian fit was made to the emergent peak in the DE2 ADC spectrum for each energy range, as shown in Figure 5-6. This fit was used cut out events with a DE2 ADC value outside of an acceptable range. This range was defined as $\pm 2.576\sigma$ from the mean of the Gaussian fit, where σ is the standard deviation of the Gaussian fit in channels. This range would contain 99% of the real events if the Gaussian fit perfectly fit the data.

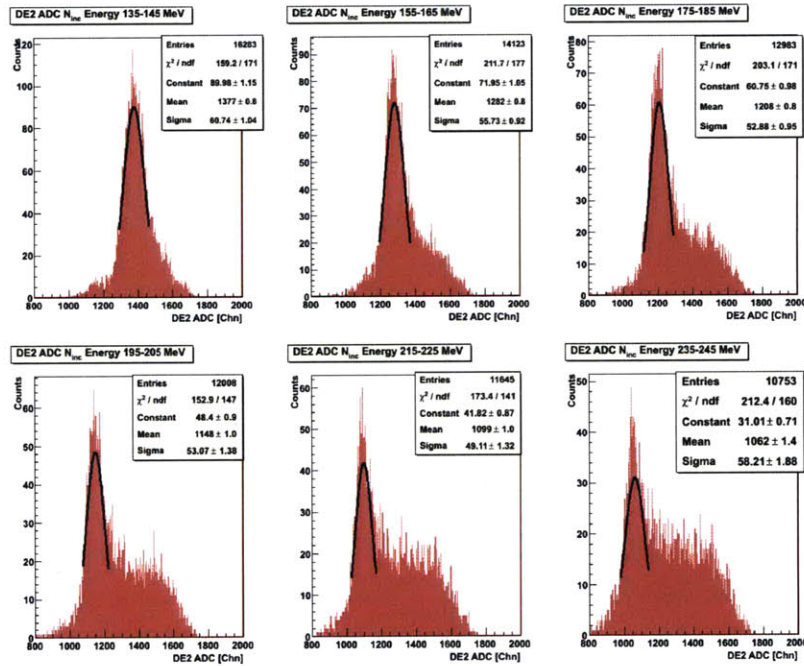


Figure 5-6: DE2 ADC spectrum for liquid deuterium target after the graphical deuteron cut in Figure 5-1 is applied for 6 different cuts on 10 MeV ranges of incident neutron kinetic energy.

5.3.2 CsI ADC Cut for Elastically Scattered Deuterons

The next step was to make a cut based on the ADC spectrum of the CsI detector, after having applied the cut such that the DE2 ADC value was within $\mu_{DE2} \pm 2.576\sigma_{DE2}$, where μ_{DE2} is the centroid and σ_{DE2} is the standard deviation of the DE2 Gaussian fit. A peak emerges in the CsI ADC spectrum, and a Gaussian is fit to this peak. This

Table 5.1: DE2 ADC when the target is filled with liquid deuterium.

N_{inc} Energy [MeV]	DE2 Gaussian Fit Mean [Chn]	DE2 Gaussian Fit Standard Deviation (σ) [Chn]
135-145	1377	60.74
155-165	1282	55.73
175-185	1208	52.88
195-205	1148	53.07
215-225	1099	49.11
235-245	1062	58.21

Table 5.2: DE2 ADC cuts when the target is filled with liquid deuterium.

N_{inc} Energy [MeV]	DE2 ADC Min [Chn]	DE2 ADC Max [Chn]	Detected Deuterons [Counts]	Detected Deuterons Between DE2 ADC Min and DE2 ADC Max [Counts]
135-145	1221	1533	16283	14392
155-165	1138	1426	14123	10925
175-185	1072	1344	12983	8820
195-205	1011	1285	12008	7120
215-225	972	1226	11645	5947
245-245	912	1212	10753	5500

fit is shown in Figure 5-7. A narrower cut of $\mu \pm 1.645\sigma$, where μ is the centroid and σ is the standard deviation of the CsI Gaussian fit in channels. This cut would contain 90% of the real events if the Gaussian fit perfectly fit the data. This is accounted for by dividing by 0.9, as shown in Equation 5.1. The counts within this peak are considered the number of detected elastically scattered deuterons.

$$D = D_{InRange} \cdot \frac{1}{0.9} \quad (5.1)$$

where D is the number of elastically scattered deuterons, the factor $\frac{1}{0.9}$ is applied because only 90% of the counts are within ± 1.645 standard deviations of the centroid of a Gaussian fit, and $D_{InRange}$ is given by Equation 5.2.

$$D_{InRange} = \mu \pm 1.645\sigma \quad (5.2)$$

where μ is the centroid channel of a Gaussian fit to a peak in the CsI ADC spectrum shown in Figure 5-7, and σ is the standard deviation of this fit in channels.

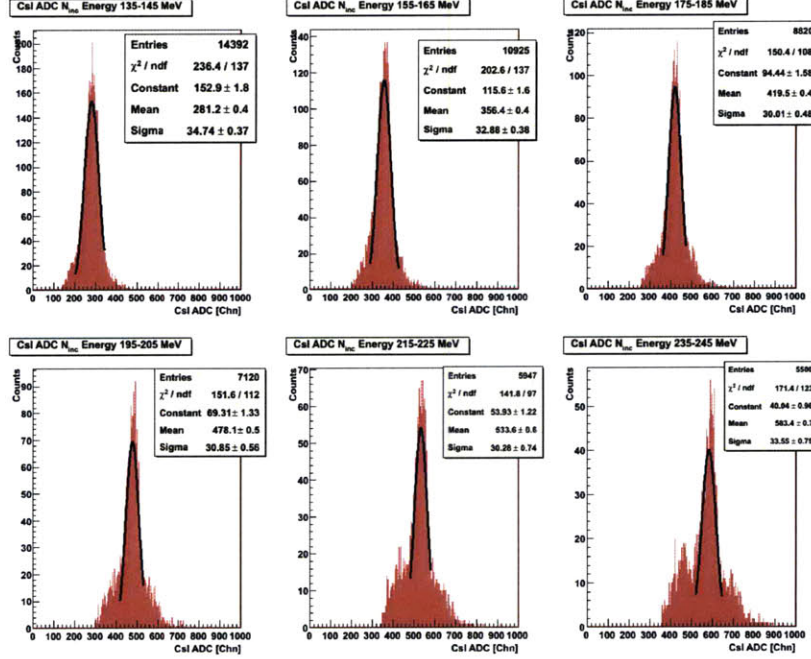


Figure 5-7: The CsI ADC spectrum shown for runs when the target was filled with liquid deuterium after the following cuts have been made: elastic trigger, deuteron graphical cut shown in Figure 5-1, an incident neutron in one of six different 10 MeV energy ranges, and the DE2 ADC cut described in Section 5.3.1.

Table 5.3: CsI ADC Gaussian fit parameters when the target is filled with liquid deuterium.

N_{inc} Energy [MeV]	CsI Gaussian Fit Mean [Chn]	CsI Gaussian Fit Standard Deviation (σ) [Chn]
135-145	281	34.74
155-165	356	32.88
175-185	420	30.01
195-205	478	30.85
215-225	534	30.28
235-245	583	33.55

Table 5.4: CsI ADC cuts when the target is filled with liquid deuterium.

N_{inc} Energy [MeV]	CsI ADC Min [Chn]	CsI ADC Max [Chn]	Deuterons in DE2 ADC Cut [Counts]	Deuterons in DE2 ADC Cut Between CsI ADC Min and CsI ADC Max [Counts]
135-145	224	338	14392	12073
155-165	302	410	10925	8638
175-185	371	469	8820	6464
195-205	427	529	7120	4914
215-225	484	584	5947	3804
245-245	528	638	5500	3162

5.4 Determination of Background in Elastically Scattered Deuteron Detection

Neutron-proton (np) scattering off of the target flask windows accidental coincidences between the CsI and DE2 detectors produce background in the detection of elastically scattered deuterons. The background from np -scattering can be accounted for by repeating the above analysis when the target is not filled with liquid deuterium, but is instead empty. The number of counts is then scaled by the number of fission events to account for the events in the full target run which were background events, as shown by Equation 5.3.

$$BG_{full} = BG_{empty} \frac{N_{full}}{N_{empty}} \frac{l_{empty}}{l_{full}} \quad (5.3)$$

where BG_{full} is the background events for runs in which the target was filled with liquid deuterium, BG_{empty} is the background for runs in which the target was empty, N_{empty} is the number of incident neutrons as determined by the fission chamber for runs in which the target was empty, and N_{full} is the number of incident neutrons as determined by the fission chamber for the runs in which the target was filled with liquid deuterium, l_{empty} is the live time of the data acquisition system (DAQ) when the target was empty and l_{full} is the live time of the DAQ when the target was full.

Both l_{empty} and l_{full} were assumed to be unity, further analysis will be performed to determine the validity of this assumption.

A check of the validity of the deuteron identification process described in Section 5.3 is to view this cut for the empty target runs. Figure 5-8 shows the lack of a deuteron band, and a less pronounced proton band, when compared with Figure 5-1. Similarly Figure 5-9 and Figure 5-10 show the lack of an emerging peak for empty target runs when compared with Figure 5-6 and Figure 5-7.

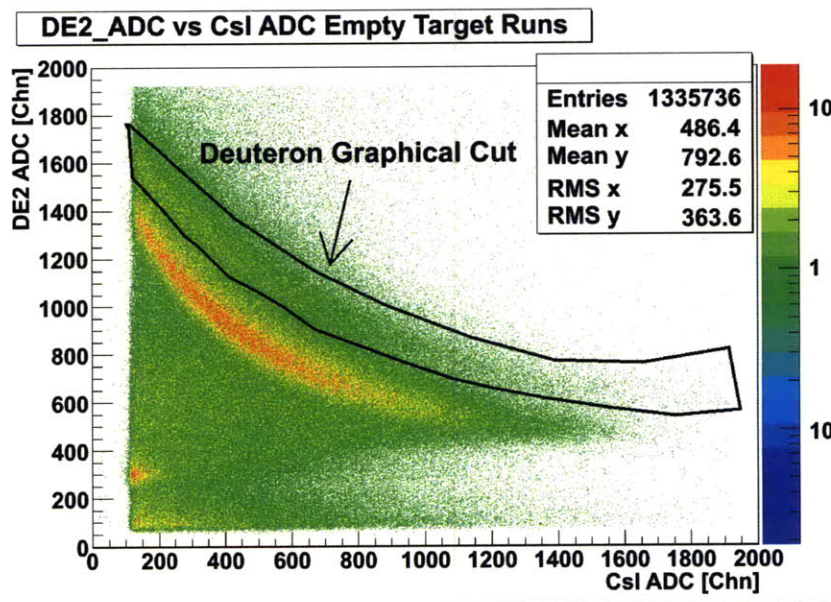


Figure 5-8: The DE2 ADC value plotted against the Csi ADC value when the target is empty

For empty target runs, there were $2.56 \cdot 10^7$ triggers in total. Of these $1.34 \cdot 10^6$ were elastic triggers, which required a t_0 pulse and a coincidence between the CsI and DE2 detectors. Of the elastic triggers $1.30 \cdot 10^5$ were in the graphical deuteron cut shown in Figure 5-8.

The incident neutron flux is determined as described in Section 3.4, and shown in Table 5.6.

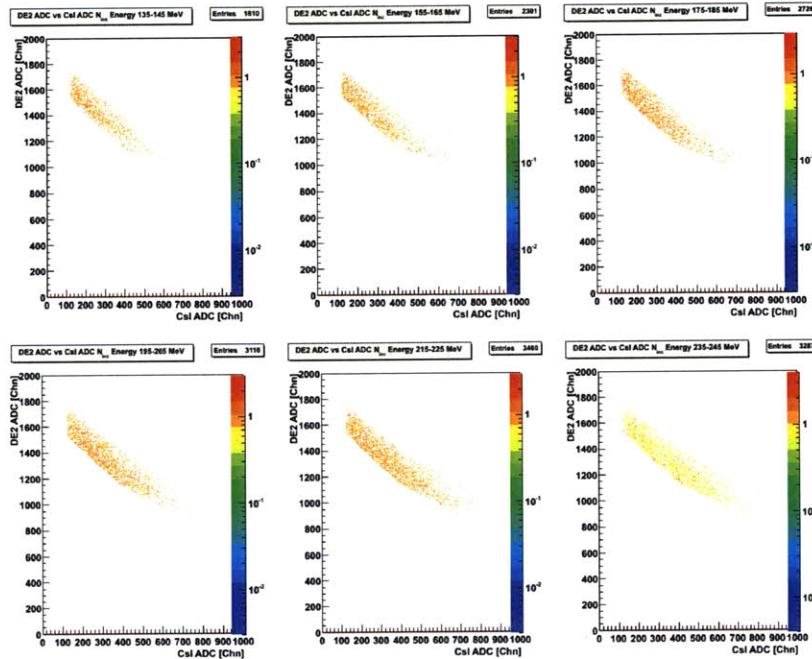


Figure 5-9: DE2 vs CsI ADC spectra for empty target runs when the graphical deuteron cut in Figure 5-1 is applied for 6 different cuts on 10 MeV ranges of incident neutron kinetic energy are made.

Table 5.5: Empty target events identified as deuterons.

N_{inc} Energy [MeV]	Deuterons in Graphical Cut shown in Figure 5-1 [Counts]	Deuterons in DE2 ADC Cut Between CsI ADC Min and CsI ADC Max [Counts]
135-145	1810	567
155-165	2301	534
175-185	2726	415
195-205	3116	431
215-225	3460	354
245-245	3287	356

5.5 Alternative Method for Determining Background in Scattered Deuteron Determination

Another way of estimating the background in the elastically scattered deuteron determination process is to estimate the number of counts away from the centroid in

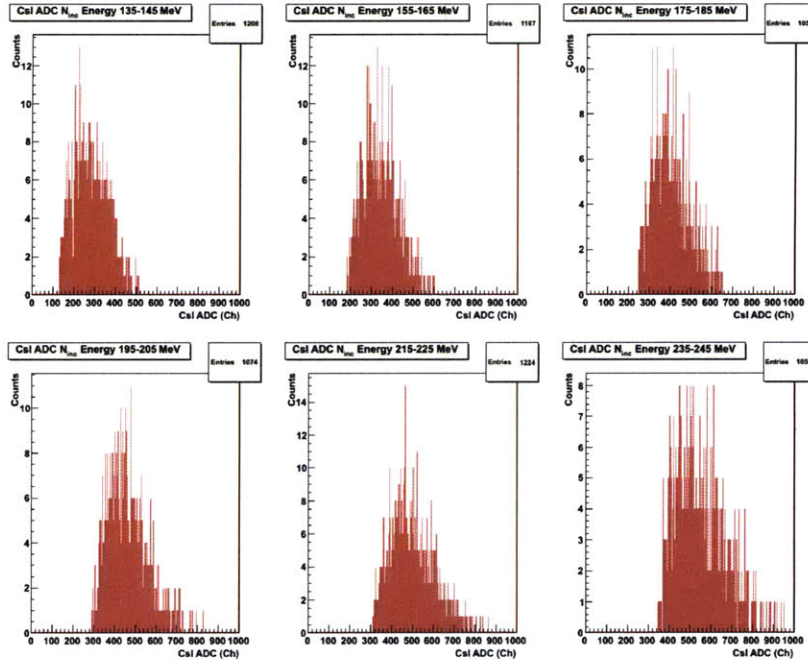


Figure 5-10: The CsI ADC spectrum shown for runs when the target was empty after the following cuts have been made: elastic trigger, deuteron graphical cut shown in Figure 5-1, an incident neutron in one of six different 10 MeV energy ranges, and the DE2 ADC cut described in Section 5.3.1

Table 5.6: Incident neutron flux and number of detected deuterons.

N_{inc} Energy [MeV]	N_{inc} for Liquid Deuterium Target [Counts]	N_{inc} for Empty Target [Counts]	Scaled Background [Counts]	Real Counts - Scaled Background
135-145	$8.054 \cdot 10^{10}$	$2.967 \cdot 10^{10}$	1539	10534
155-165	$7.549 \cdot 10^{10}$	$2.798 \cdot 10^{10}$	1441	7187
175-185	$6.978 \cdot 10^{10}$	$2.592 \cdot 10^{10}$	1117	5346
195-205	$6.410 \cdot 10^{10}$	$2.395 \cdot 10^{10}$	1154	3760
215-225	$5.998 \cdot 10^{10}$	$2.207 \cdot 10^{10}$	954	2842
245-245	$5.590 \cdot 10^{10}$	$2.103 \cdot 10^{10}$	946	2216

Figure 5-7. The advantage of this method is that it does not rely on the experimental setup being the same for empty target and liquid deuterium target runs. The disadvantage of this method is that it is more dependent on the accuracy of the Gaussian fit to the CsI ADC spectrum. This method uses the DE2 ADC cut shown in Table 5.2. However, instead of making the CsI ADC acceptance range is within $\mu \pm 1.645\sigma$

(where μ is the centroid of the Gaussian fit and σ is the standard deviation of this fit) and then dividing by 0.9 as in Section 5.3.2, the acceptance range is $\mu \pm 2.576\sigma$. The primary difference however is that it assumes that counts at 2.576σ are due entirely to background. This background is then estimated by taking the average number of counts in a 10 channel wide cut around the channels which are $\mu \pm 2.576\sigma$ (rounded to the nearest channel). It was found that the lower channels always had more background; for simplicity, a linearly declining background was assumed. This was then used to estimate the background as shown in Equation 5.4. This data is presented in Table 5.7.

$$BG = CsI_{Range} \cdot \left(r_{BG} + \frac{l_{BG} - r_{BG}}{2} \right) \quad (5.4)$$

where BG is the number of background counts, CsI_{Range} is the number of channels within $\pm 2.576\sigma$ of the centroid of the Gaussian fit shown in Figure 5-7, r_{BG} is the average number of counts within ± 5 channels of the channel that is closest to $\mu + 2.576\sigma$, l_{BG} is the average number of counts within ± 5 channels of the channel that is closest to $\mu - 2.576\sigma$.

Table 5.7: Alternative background determination for elastically scattered deuteron determination.

N_{inc} Energy [MeV]	Low Channel Background [Counts]	High Channel Background [Counts]	Total Background in CsI cut [Counts]	Total Counts in CsI cut	Counts with Background Subtracted
135-145	19.7	9.8	2614	13758	11144
155-165	14.8	13	2487	10197	7710
175-185	15.7	11.1	2216	7789	5573
195-205	13.2	12.4	2066	5834	3768
215-225	13	8.3	1645	4567	2922
245-245	10.8	6.3	1530	3836	2306

The majority of the background comes from np -scattering off the liquid deuterium chamber; therefore this background should not change whether or not the target is filled with liquid deuterium [4]. The alternative method of background determination

was compared to the background discussed in Section 5.4 to check the validity of this assumption, as discussed in Chapter 6.

5.6 Energy Loss in Target

As described in Section 4.5, the energy lost in the target causes an underestimation of the effective target thickness, x_{eff} if it is not accounted for. It was found that accounting for energy lost in the target did in fact raise x_{eff} .

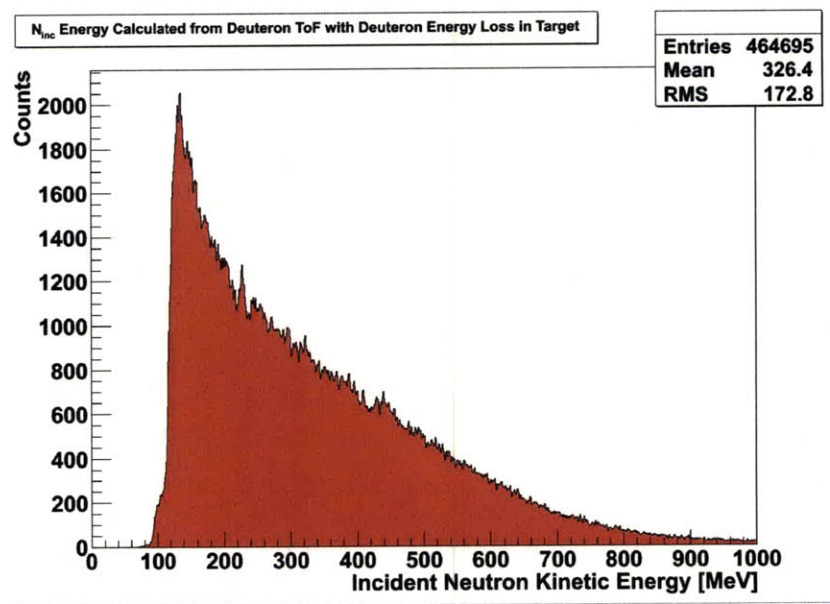


Figure 5-11: Incident neutron energy determined by total time of flight of the incident neutron and scattered deuteron as described in Section 4.5. This accounts for energy lost by the elastically scattered deuteron in the liquid deuterium target.

The process described in Section 5.3 was repeated accounting for energy loss.

The background was determined using empty target runs, as described in Section 5.4. The results are presented in Table 5.12.

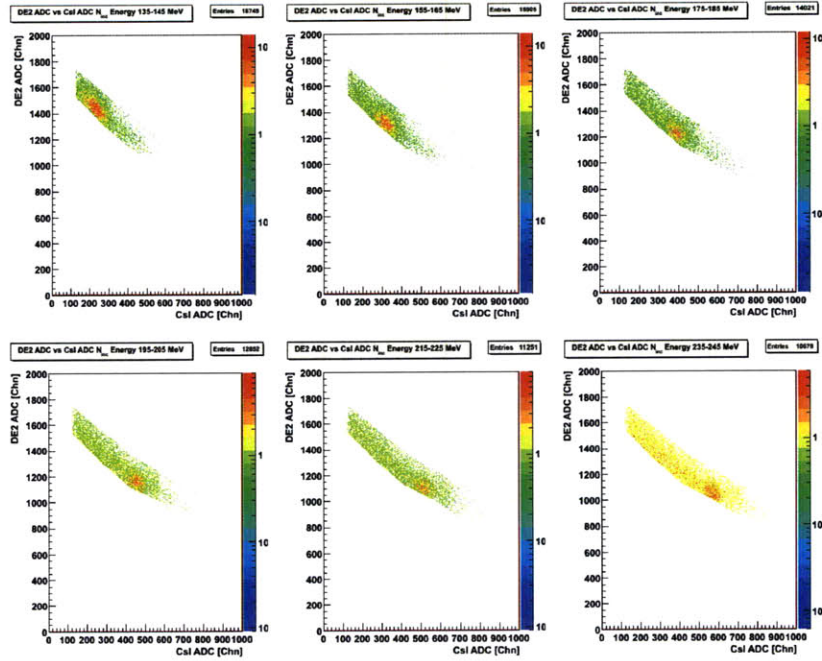


Figure 5-12: DE2 vs CsI ADC spectra when the graphical deuteron cut in Figure 5-1 is applied for 6 different cuts on 10 MeV ranges of incident neutron kinetic energy are made (calculated with total time of flight of the neutron and scattered deuteron accounting for energy lost in the liquid deuterium target).

Table 5.8: DE2 ADC when the target is filled with liquid deuterium and energy loss is accounted for when determining N_{inc} energy.

N_{inc} Energy [MeV]	DE2 Gaussian Fit Mean [Chn]	DE2 Gaussian Fit Standard Deviation (σ) [Chn]
135-145	1450	66.22
155-165	1326	55.25
175-185	1238	53.35
195-205	1171	53.38
215-225	1120	56.01
235-245	1074	59.06

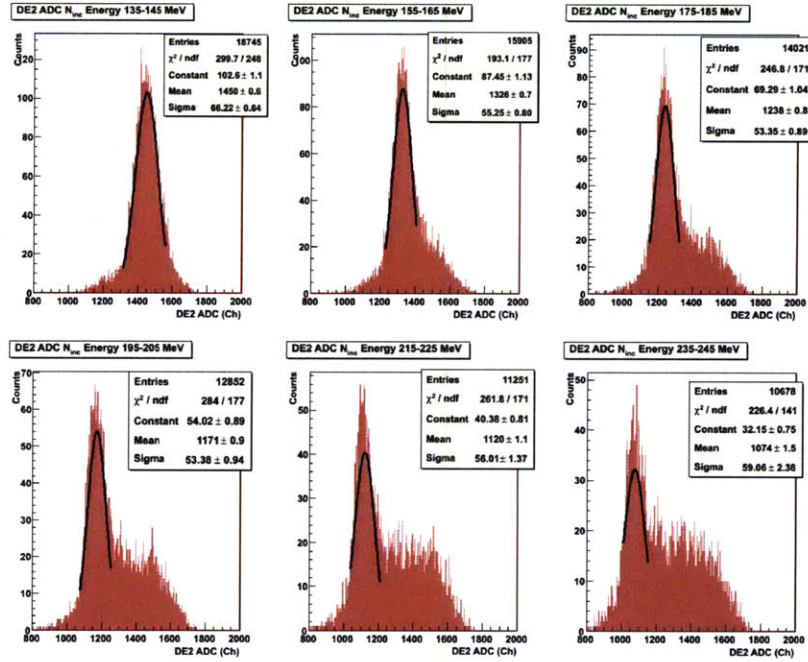


Figure 5-13: DE2 ADC spectrum for liquid deuterium target after the graphical deuteron cut in Figure 5-1 is applied for 6 different cuts on 10 MeV ranges of incident neutron kinetic energy (calculated with total time of flight of the neutron and scattered deuteron accounting for energy lost in the liquid deuterium target).

Table 5.9: DE2 ADC cuts when the target is filled with liquid deuterium and energy loss is accounted for when determining N_{inc} energy.

N_{inc} Energy [MeV]	DE2 ADC Min [Chn]	DE2 ADC Max [Chn]	Detected Deuterons [Counts]	Detected Deuterons Between DE2 ADC Min and DE2 ADC Max [Counts]
135-145	1279	1621	18745	17662
155-165	1184	1468	15905	13050
175-185	1101	1375	14021	10164
195-205	1033	1309	12852	8170
215-225	976	1264	11251	6344
245-245	922	1226	10678	5654

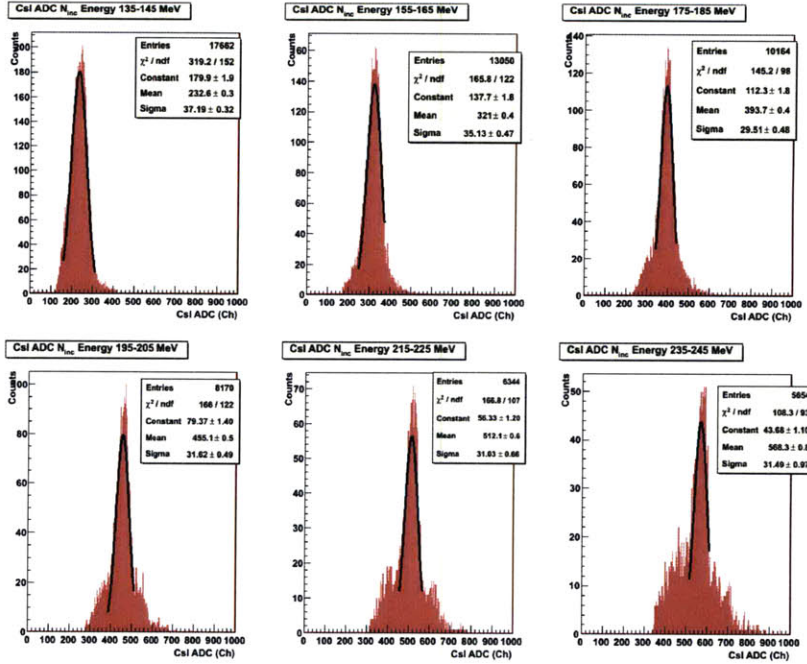


Figure 5-14: The CsI ADC spectrum shown for runs when the target was filled with liquid deuterium after the following cuts have been made: elastic trigger, deuteron graphical cut shown in Figure 5-1, an incident neutron in one of six different 10 MeV energy ranges (accounting for energy loss in the target), and the DE2 ADC.

Table 5.10: CsI ADC Gaussian fit parameters when the target is filled with liquid deuterium and energy loss is accounted for when determining N_{inc} energy.

N_{inc} Energy [MeV]	CsI Gaussian Fit Mean [Chn]	CsI Gaussian Fit Standard Deviation (σ) [Chn]
135-145	232.6	37.19
155-165	321.4	35.13
175-185	393.7	29.51
195-205	455.1	31.62
215-225	512.1	31.03
235-245	568.3	31.49

Table 5.11: CsI ADC cuts when the target is filled with liquid deuterium and energy loss is accounted for when determining N_{inc} energy.

N_{inc} Energy [MeV]	CsI ADC Min [Chn]	CsI ADC Max [Chn]	Deuterons in DE2 ADC Cut [Counts]	Deuterons in DE2 ADC Cut Between CsI ADC Min and CsI ADC Max [Counts]
135-145	171	294	17662	15283
155-165	264	379	13050	10895
175-185	345	442	10164	7615
195-205	403	507	8170	5745
215-225	461	563	6344	4058
245-245	517	620	5654	3169

Table 5.12: Incident neutron flux and number of detected deuterons.

N_{inc} Energy [MeV]	N_{inc} for Liquid Deuterium Target [Counts]	N_{inc} for Empty Target [Counts]	Scaled Background [Counts]	Real Counts - Scaled Background
135-145	$8.054 \cdot 10^{10}$	$2.967 \cdot 10^{10}$	1933	13350
155-165	$7.549 \cdot 10^{10}$	$2.798 \cdot 10^{10}$	1541	9354
175-185	$6.978 \cdot 10^{10}$	$2.592 \cdot 10^{10}$	1303	6312
195-205	$6.410 \cdot 10^{10}$	$2.395 \cdot 10^{10}$	1154	4592
215-225	$5.998 \cdot 10^{10}$	$2.207 \cdot 10^{10}$	1071	2987
245-245	$5.590 \cdot 10^{10}$	$2.103 \cdot 10^{10}$	872	2297

Chapter 6

Results and Error Analysis

6.1 Value of Effective Target Thickness

The process described in Chapter 5 was used to determine the effective target thickness, x_{eff} , using three methods: determining incident neutron energy from total time of flight of the neutron and elastically scattered deuteron without accounting for energy loss of the deuteron in the liquid deuterium target and using either the background as determined in Section 5.4 or the background as described in Section 5.5, determining neutron energy from total time of flight of the neutron and elastically scattered deuteron accounting for energy loss of the deuteron in the liquid deuterium target and using the background as determined in Section 5.4. The results of these three methods are presented in Table 6.1 and Table 6.2.

As discussed in Section 4.1 the physical target thickness, x_{phy} is 1.1 in. Although x_{eff} could deviate from this value, this measurement is thought to be an upper limit on the effective thickness of the target. The effect of bubbling of the liquid deuterium decreases the density of the target and thus decreases x_{eff} relative to x_{phy} . If the target was at a large angle with the beam this should have been noticed (the window to the target was transparent). Regardless of the method used to determine x_{eff} , the value of x_{eff} is over 3.5 standard deviations away from the upper limit set by the physical target thickness measured while the target was at a gauge pressure of 14 psi (although the target was not filled with liquid deuterium when this measurement

Table 6.1: Effective target thickness determined as described in Chapter 5.

Energy [MeV]	x_{eff} No Energy lost in target [in]	x_{eff} Alternative Background (no energy lost) [in]	x_{eff} With Energy Loss in Target [in]
135-145	1.8	1.8	2.3
155-165	1.8	1.7	2.3
175-185	2.2	2.1	2.6
195-205	2.1	1.9	2.6
215-225	2.1	1.9	2.2
245-245	1.9	1.7	1.9

Table 6.2: Mean and standard deviation of the values of the effective target thickness calculated for the 6 energy ranges shown in Table 6.1.

Method	x_{eff} Average [in]	x_{eff} Standard Deviation [in]
No energy lost in target	2.0	0.2
No energy lost in target alternative background	1.9	0.2
Energy lost in target	2.3	0.3

was made). This strongly suggests that there is an error either in how the data was acquired or in how the data was analyzed.

There are a few factors which could raise x_{eff} relative to the values determined in this thesis, driving it even further away from the upper bound of 1.1 in. One assumption made in this analysis was that the live time of the data acquisition system (DAQ) was 1.0; it is probable that this live time is actually closer to 0.8, as in [4]. When calculating the energy lost by the deuteron, described in Section 4.5, only the energy lost in the liquid deuterium target was taken into account. The deuteron also loses energy on other stages of its flight path, as discussed in [4], if this energy lost was accounted for it would also increase the value of x_{eff} .

It is possible the determination of background, discussed in Section 5.4, was not performed correctly. However, when an alternative background was used, as in Sec-

tion 5.5, the value of x_{eff} was still unphysically large. Another possible explanation for the unphysical value of x_{eff} is that the incident neutron flux, N_{inc} , described in Chapter 3, was not determined correctly. The fission chamber was assumed to be the same fission chamber used in [2] and [4]; however, it is possible that this assumption is not valid. If this assumption is not valid, the thickness of the ^{238}U foils of the fission chamber used in the analysis could be incorrect, leading to a too low determination of N_{inc} , which would cause an overestimation of x_{eff} .

One potential source of error in this experiment that will be investigated in the future is drift in either the CsI or the DE2 ADC or TDC. There is a method of determining drift of the TDC calibration in this experiment, discussed in [10], that was not used in the analysis described in this thesis. Similarly it is possible that either the CsI or the DE2 ADC could have drifted over time. When analysis similar to that described in Chapter 5 was performed on the first half of liquid deuterium runs, the value of x_{eff} did not drop below 1.1 in. However, this analysis was performed quickly; in the future it will be performed more carefully.

This thesis followed an analysis process very similar to the analysis described in [4]. However, one important difference is that in [4], both the scattered deuteron and the scattered neutron were detected. This allowed the author of [4] an additional piece of information in the identification of deuterons that was not available in the experiment described in this thesis. It is possible that the detection of this scattered neutron helps discriminate against a type of background that neither method of background determination used in this thesis is sensitive to.

The value of x_{eff} could be checked using the data acquired when the target was filled with liquid hydrogen. Although the fission chamber did not function during these runs, the flux of incident neutrons could be determined by measuring the cross section of np -scattering with techniques similar to those described in [10]. This analysis is beyond the scope of this thesis.

6.2 Error Analysis

The standard deviation of the values of x_{eff} determined for each of the 6 different energy ranges is a good measure of the total error associated with this experiment. The standard deviation suggests a relative error of about 10 percent on the determined value of x_{eff} . The dominant sources of known error in the determination of x_{eff} come from the fission chamber and the nd -scattering cross section. The relative error on the fission chamber is given as 8% by [4] and 10% by [2]. The relative error on the nd -scattering cross section is 10%, as shown in Table 4.1. However, these two sources of error may not be independent because the determination of the nd -scattering cross section used a fission chamber similar to the one used in this experiment, as described by [4].

There is a statistical error of 2% from the determination of the background. This is given by $\frac{1}{BG^5}$, where BG is the sum of background counts for all energy ranges, determined in Section 5.4. However, the number of counts from scaled background is about one sixth the total number of counts, which decreases the effect error on the background has on the determination of x_{eff} . The statistical error of the detected deuterons is less than 1%. This is given by $\frac{1}{N_D^5}$, where N_D is the total number of detected deuterons at all energy ranges.

Chapter 7

Conclusion

A method of determining the effective target thickness of a liquid deuterium target was discussed in this thesis. The effective target thickness was determined by measuring the yield of detected deuterons which were elastically scattered by neutrons. The effective target thickness determined was larger than believed possible. Some possible explanations for this result were discussed; however, further analysis is needed to determine what the cause of this error actually is. This analysis is outside the scope of this thesis, but will likely be performed in the future.

Appendix A

Electrical Schematic Diagram

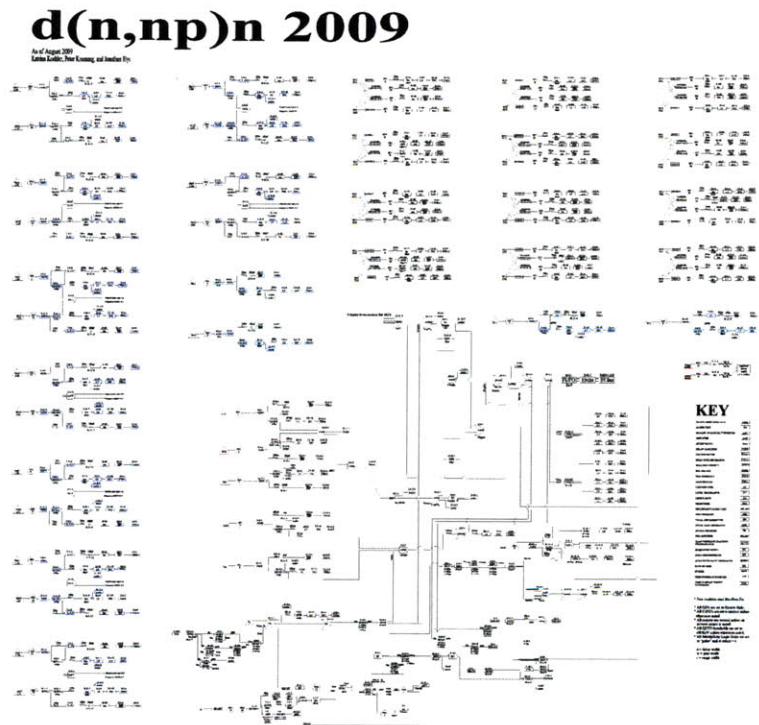


Figure A-1: Electrical schematic diagram for this experiment.

Bibliography

- [1] R. Adelberger and C. Brown. pd elastic cross section and polarization at 198 mev. *Physical Review D*, 5(9):2139, 1972.
- [2] Taylan Akdoğan. *Pion Production in the Neutron-Proton Interaction*. PhD dissertation, Massachusetts Institute of Technology, Department of Physics, September 2003.
- [3] Kimberly K. Boddy. *Charged-Particle Tracking for Neutron-Deuteron Breakup*. SB thesis, Massachusetts Institute of Technology, Department of Physics, June 2007.
- [4] Maxim B. Chtangeev. *Neutron-Deuteron Elastic Scattering and the Three-Nucleon Force*. MS dissertation, Massachusetts Institute of Technology, Department of Physics, June 2005.
- [5] A. Jablonski. Elastic scattering of electrons and positrons. *Journal of the ICRU*, 7(1), 2007.
- [6] William R. Leo. *Techniques for Nuclear and Particle Physics Experiments: A How-to Approach*, Section 2.2.2. Springer-Verlag, Berlin, first edition, 1987.
- [7] Alice E. Ohlson. *Neutron-Deuteron Breakup and Quasielastic Scattering*. SB thesis, Massachusetts Institute of Technology, Department of Physics, June 2009.
- [8] W. Pairsuwan, J.W. Watson, M. Ahmad, N.S. Chant, B.S. Flanders, R. Madey, P.J. Pella, and P.G. Roos. Analyzing powers for the ${}^2H(p,pn){}^1H$ reaction at 200 MeV. *Physical Review C*, 52(5):2552–2558, November 1995.
- [9] F. Takeutchia, T. Yuasaa, K. Kurodaa, and Y. Sakamotoa. Experimental test of the impulse approximation in the $2h(p, 2p)n$ reaction. *Nuclear Physics A*, 152(2):434–448, 1970.
- [10] Sho Uemura. *Differential Cross Section Measurement for the $d(n,np)$ Reaction*. SB thesis, Massachusetts Institute of Technology, Department of Physics, June 2010.
- [11] S. A. Wender, S. Balestrini, A. Brown, R. C. Haight, C. M. Layman, T. M. Lee, P. W. Lisowski, W. McCorkle, R. O. Nelson, and W. Parker. A fission

ionization detector for neutron flux measurements at a spallation source. *Nuclear Instrumentation and Methods in Physics Research*, 336:226231, 1993.